New constraints from Central Chile on the origins of enriched continental compositions in thick-crusted arc magmas

Penny E. Wieser[1,2*], Stephen J. Turner[3], Tamsin A. Mather[1], David M. Pyle[1], Ivan P. Savov[4] and Gabriel Orozco[5]

[1] Department of Earth Sciences, University of Oxford, South Parks Road, Oxford OX1 3AN, UK
[2] Now at Department of Earth Sciences, University of Cambridge, Downing Street, Cambridge, UK, CB2 3EQ.
[3] Washington University in St. Louis, One Brookings Drive, St. Louis, MO 63130
[4] School of Earth and Environment, Institute of Geophysics & Tectonics, University of Leeds, Leeds LS2 9JT, UK.
[5] Red Nacional de Vigilancia Volcánica, Servicio Nacional de Geología y Minería, Av. Santa María 0104, Providencia, Chile.

* Corresponding author: pew26@cam.ac.uk. Phone: 07593670818

Abstract

Volcanics from thick-crusted continental arcs have elevated incompatible element abundances and "enriched" radiogenic isotope ratios compared to volcanics erupted in island arcs and continental arcs with thinner crust. The relative influence of the slab, mantle, and upper plate on this variability remains debated. The Andean Southern Volcanic Zone (SVZ; 33-46° S) is an ideal setting to investigate the production of enriched continental arc volcanics, because both crustal thickness and magma chemistry show coherent along-strike variations. However, the scarcity of primitive volcanism in the thick-crusted northern SVZ has hindered previous regional studies. To better address the origin of enriched continental compositions, this study investigates the geochemistry (major and trace element abundances, $^{87}Sr/^{86}Sr$ and $^{143}Nd/^{144}Nd$) of new mafic samples from Don Casimiro and Maipo volcanoes (within the Diamante-Maipo Caldera Complex of the northern SVZ). While evolved Diamante-Maipo samples show evidence for crustal assimilation, the trace element and isotopic enrichment of the most mafic samples cannot result from crustal processing, as a compilation of regional and global basement lithologies are not enriched in all of the necessary incompatible trace elements. This reflects the fact that many of the elements which are enriched in the mafic Don Casimiro-Maipo samples (e.g. Sr, Zr, P) are depleted by the various complex petrogenetic processes affecting basement lithologies (e.g. fractionation of accessory phases). Subduction erosion models similarly fail to account for the enriched isotopic and trace element signature of these samples. Instead, the enrichment of the northern SVZ is most consistent with an enriched ambient mantle component (similar to EM1-type ocean island basalts), superimposed on a northward decline in melt extent. A substantial, but nearly uniform contribution of melts from subducting sediment and altered oceanic crust are also required at all latitudes. The EM1-like enrichment may arise from recycling of metasomatized subcontinental lithospheric mantle (M-SCLM), as the isotopic trajectory of primitive rear-arc monogenetic cones trend towards the composition of SCLM melts sampled across South America. The wide spatial distribution of rear-arc centres with isotopic data clearly demonstrates that the latitudinal variations in the amount of EM1-type enrichment observed in arc-front samples are also present in the rear-arc. Rear-arc trace element systematics indicate that significant but variable quantities of slab melts are also transported to the rear-arc mantle. Overall, we show that a unified model incorporating variable mantle enrichment, slab additions, and melt extents can account for along and across arc trends within the SVZ. As subduction zones have been the loci of continental crust creation for over 2 Ga, the finding that mantle enrichment plays a dominant role in the production of enriched continental compositions in the SVZ has important implications for our understanding of the chemical evolution of the Earth. If ambient mantle enrichment is not taken into account, petrogenetic models of evolved lavas may overestimate the role of crustal assimilation, which, in turn, may lead models of continental crust growth exaggerating the amount of continental material that must be recycled back into the mantle to satisfy mass balance.

Key Words
- Mantle heterogeneity
- Andean Southern Volcanic Zone

Highlights
- NSVZ isotopic and trace element enrichment indicate an EM1-like mantle source.
- EM1-like signatures originate from recycling of M-SCLM from nearby cratons.
- Slab melting, low mantle melt extents, and M-SLCM may enrich continental arc lavas
- The slab component supplied to the rear-arc and arc-front have similar compositions.
- Slab materials are not transported vertically to the wedge from their point of origin.

1. Introduction

Magmas which erupt from continental arc-front stratovolcanoes are compositionally distinct from oceanic arc magmas. With the exception of volcanics from intra-arc rift zones (e.g. Conrey and Schmidt, 2004), these continental magmas exhibit elevated incompatible element abundances, steeper incompatible trace element patterns (Fig. 1a), and often have isotopic signatures offset to higher ^{87}Sr/^{86}Sr and lower ^{143}Nd/^{144}Nd than oceanic arc magmas (Leeman et al., 1983; Plank and Langmuir, 1988; Hildreth and Moorbath, 1988; Turner and Langmuir, 2015a; Farner and Lee, 2017). Many of these compositional characteristics correlate strongly with crustal thickness (Turner et al., 2015a), and have been used as proxies to estimate changes in crustal thickness and rates of surface uplift though time (Profeta et al., 2015; Chiaradia, 2015; Chapman et al., 2015; Scott et al., 2018). Some of the compositional offsets between thick and thin-crusted arcs can be accounted for by higher extents of crystal fractionation and crustal assimilation in continental settings (e.g. Farner and Lee, 2017). However, other compositional differences persist in high Mg# arc lavas (Fig. 1a) that have not been extensively overprinted in the crust (e.g. Plank and Langmuir, 1988; Turner and Langmuir, 2015a; Turner et al., 2017; Schmidt and Jagoutz, 2017), suggestive of a mantle origin. Compositional differences among parental magmas from continental vs. oceanic arc settings have been attributed to variations in slab temperature (Ruscitto et al., 2012; Turner and Langmuir, 2015b; Schmidt and Jagoutz, 2017), different extents of mantle melting (e.g. Plank and Langmuir, 1988; Tormey et al., 1991; Turner et al., 2016), subduction erosion (e.g. Stern, 1989), and heterogeneity of the “ambient” mantle (the mantle prior to the addition of subducted materials, e.g. Hickey et al., 1986; Ewart and Hawkesworth, 1987; Rogers and Hawkesworth, 1989; Hochstaedter et al., 2001; Pearce et al., 2007; Turner et al., 2017). Furthering our understanding of the thermal structures of subducting plates, the growth of the continental crust, and the petrogenesis of evolved arc magmas requires constraints on the relative influence of each factor in producing the enriched compositions of continental arc magmas.

The Andean Southern Volcanic Zone (SVZ) is an excellent natural laboratory in which to investigate how the thick crusts and lithospheres of active compressional plate margins affect the compositions of magmas added to the continents. The SVZ (33-46° S) is one of four volcanically active segments within the Andean Cordillera, where the Nazca Plate subducts under South America. It is commonly subdivided into three sub-segments: the northern, transitional, and southern SVZ (NSVZ, TSVZ and SSVZ respectively; Dungan et al., 2001; Fig. 2a). From the easily-accessed segments of the SSVZ to the NSVZ (42° S to 33° S), crustal thickness increases from ~30 to 50 km (Fig. 2c), sub-arc slab depth increases from ~70 to 120 km (Tassara and Echaurren, 2012), and the lower plate age increases from 16 to 37 Ma (Völker et al., 2011), while trench sediment thickness decreases (Völker et al., 2013). In the NSVZ, seismic and heat flow data indicate that the lithosphere thickness increases rapidly behind the arc, while behind the SSVZ, the lithosphere is thinner (Tassara and Echaurren, 2012; Valdenegro et al., 2019). As a result, the mantle wedge in the NSVZ is colder and deeper (Turner et al., 2016). There are also well-established geochemical gradients from the SSVZ to the NSVZ (Tormey et al., 1991; Hildreth and Moorbath, 1988; Hickey et al., 2016, Fig. 2d-e). The trace element signatures of mafic SSVZ volcanics overlap those of oceanic arcs (Fig. 1a). In contrast, the more mafic TSVZ lavas have substantially elevated trace element abundances. The limited amount of trace element data from mafic NSVZ lavas (Fig. 1a; Hickey et al., 1986) demonstrates that this segment is even more enriched than the TSVZ, with compositions similar to the bulk continental crust and mafic to intermediate volcanics from other thick-crusted arc segments such as the Northern Cascades (Fig. 1a). Thus, the chemical variability between the SSVZ and NSVZ is analogous to the chemical offsets between island arcs, continental arcs, and the bulk continental crust.

While many studies have investigated the origin of along-strike compositional variability of the SVZ arc-front volcanoes (Lopez-Escobar et al., 1977; Hickey et al., 1986; Hildreth and Moorbath, 1988; Tormey et al., 1991; Jacques et al., 2014; Hickey et al., 2016), the role of enrichment and heterogeneity within the ambient asthenospheric mantle (prior to the addition of subducted material) has received relatively little attention (Hickey et al., 1986; Jacques et al., 2014). Though often overlooked, the extent to which the compositions of continental arc volcanics are inherited from the ambient mantle has important implications for models of crustal growth. If the trace element enrichment of continental arcs is inherited partially from the mantle, and not exclusively from extensive crystal fractionation and crustal remelting, a substantially smaller amount of material must be returned to the mantle to account for the continental mass balance (e.g. Sisson and Keleman, 2018). The amount of crustal recycling, in turn, has direct relevance for our understanding of the generation of large-scale mantle heterogeneity.

Heterogeneity of the upper mantle is commonly inferred from trace element and isotopic compositions of mid-oceanic ridge basalts (MORBs) and ocean island basalts (OIBs; Zindler and Hart, 1986; Willbold and Stracke, 2010). OIB isotopic variability can be generally be accounted for by a handful of isotopically distinct end-member components, such as the “enriched mantle” end-members (EM1, EM2; e.g. Zindler and Hart, 1986). Isotopic end-members are often modelled as the products of recycled lithospheric mantle, sediment, and ancient oceanic/continental crust (Willbold and Stracke, 2010). There is also evidence for heterogeneity in the ambient mantle that feeds volcanic arcs, despite additional tectonic complexity. For example, a global compilation of samples from rear-arc provinces, filtered to minimize slab contributions (Turner and Langmuir, 2015b), form a linear array between Depleted MORB Mantle (DMM) and EM-1 type OIB compositions (Fig. 3a). As corner flow transports the mantle feeding rear-arc volcanism over hundreds of kilometres towards the arc-front (MacDougall et al., 2017), isotopic enrichment within rear-arc provinces indicates that ambient sub-arc mantle compositions also vary substantially (e.g. Woodhead et al., 2012). The

Andean Southern Volcanic Zone (SVZ) rear arc exemplifies this enriched ambient mantle signature (Kay et al., 2013; Jacques et al. 2013, 2014; Søager et al., 2015a; Turner et al. 2017), with more enriched $^{87}Sr/^{86}Sr$ and $^{143}Nd/^{144}Nd$ ratios than any other rear-arc province globally (Fig. 3a).

This study investigates the petrogenesis of mafic lava samples from the volcanoes Don Casimiro and Maipo (within the Diamante-Maipo Caldera complex; 34˚S, Fig. 2b) in order to determine the geochemical character of high Mg# NSVZ magmas. These lavas from Don Casimiro and the basal portion of Maipo, which erupted immediately after the catastrophic formation (~150 ka) of the Diamante Caldera (Orozco et al., 2015), are among the most primitive ever sampled within the NSVZ (Fig. 4a; Hickey et al., 1986). Their primitive nature may indicate that the storage and eruption of these melts preceded the re-organization and maturation of crustal magma reservoirs beneath the Diamante caldera (analogous to post collapse lavas at Campi Flegrei; Forni et al., 2018), or that ascending magmas utilized tension cracks formed during the collapse event (Jacques et al., 2014). Regardless of the exact mechanism permitting the eruption of mafic lavas within the thick-crusted NSVZ, these new samples provide an opportunity to rigorously characterise and explore the origins of the prominent chemical differences between the SSVZ and the NSVZ. As the chemical variability between the SSVZ and NSVZ is analogous to the chemical offsets between island arcs and continental arcs, exploring these regional trends provides constraints on origins of magmatic enrichment within a thickened continental subduction zones globally.

This study also incorporates samples erupted within the last 1 Myr from seven Argentinean monogenetic cones from the Payenia Volcanic Province (34.33˚ to 35.38˚S; Folguera et al., 2009). The origin of this rear-arc volcanism, located up to 350 km behind the NSVZ arc front, remains a topic of active research. Volcanism initiated in the earliest Miocene, associated with a period of shallow slab subduction, and continued into the Holocene (Kay and Copeland, 2006; Pallares et al., 2016). In the southernmost part of Payenia, it is generally accepted that the slab steepened towards the present-day dip of 33° (Tassara and Echuarren, 2012) by 5 Ma (Kay et al., 2005). Folguera et al. (2009) suggest that volcanism propagated northwards following extensional relaxation of the San Rafael block, while Gudnanson et al. (2012) attribute the northward propagation of volcanism within the Payenia to a northward delay in slab rollback. Despite uncertainty in the chronology and mode of magmagenesis of the SVZ rear-arc, the wide spatial distribution of volcanic products, along with their relatively primitive chemistry, provide vital constraints on the composition of the ambient sub-arc mantle beneath the SVZ (Jacques et al., 2013; Turner et al., 2017).

2. Samples and methods

Six samples were collected from the basal sequence of Maipo Volcano, the active stratovolcano at the centre of the caldera, and nine from Don Casimiro Volcano, a small eroded stratovolcano located ~10 km SW of Maipo with activity restricted to preglacial times (Charrier, 1979; Fig. 2b). $^{40}Ar/^{39}Ar$ dates indicate that early activity at these centres was contemporaneous (Orozco et al., 2015). All lavas contain ubiquitous olivine and clinopyroxene phenocrysts within a glassy groundmass. The more evolved samples also contain plagioclase, oxides, and orthopyroxene (details in SIA2). Seven samples were collected from monogenetic scoria cones in the northern rear-arc (34.3 to 35.4 ˚S; Fig. 2a). Olivine, clinopyroxene, and oxide phenocrysts dominate in these scorias, with microcrysts of plagioclase and alkali feldspar, and minor apatite.

All 22 samples were powdered for whole-rock analysis with an agate ball mill at the University of Oxford. Major element analysis was conducted using a PANalytical Axios Advanced X-ray fluorescence spectrometer at the University of Leicester (Knott et al., 2016). Powders were digested in clean labs at the University of

Oxford for ICP-MS analysis. Ba and Sr were measured at a 1,200,000x dilution using a Thermo Element 2 ICP-MS, while all other trace elements were measured at a 6000x dilution on a Perkin Elmer NexION 350D quadrupole ICPMS (both at the University of Oxford). Four certified reference materials (CRMs; BCR-2, BHVO-2, AGV-2, and W-2a) were digested alongside these samples. Data was reduced using calibration curves generated from these 4 CRMs. Repeat solution analysis (n=19) and repeated digestions indicate an analytical uncertainty of <3% (<5% for Cs), and calculated values for the CRMs yield concentrations within ±5% of the preferred values (Appendix 3).

$^{87}Sr/^{86}Sr$ and $^{143}Nd/^{144}Nd$ isotope ratios were analysed for eleven samples at the University of Leeds. Following Sr and Nd purification, samples were loaded onto outgassed W (Sr) and Re (Nd) filaments, and analysed on a Thermo Scientific Triton-series multicollector mass spectrometer. NIST SRM-987, La Jolla and BHVO-2 were analysed throughout the session to monitor accuracy and precision (Appendix 3).

Olivine grains were analysed for major elements on a Cameca SXFive FEG-electron microprobe at the University of Oxford. St Johns Olivine and Fayalite were analysed as secondary standards to assess accuracy and precision. LA-ICP-MS olivine analysis was conducted at the University of Cambridge on a 193ESI Laser Ablation system coupled to a Nexion ICP-MS. Multiple secondary standards were run to monitor instrument drift, and accuracy and precision. Additional analytical details are provided in SIA3.

3. Results

The new Don Casimiro-Maipo samples are primitive calc-alkaline basaltic andesites to andesites. The whole-rock Mg#s (assuming Fe^{3+}/Fe_T=0.3; Holm et al., 2016) of Don Casimiro-Maipo samples mostly range from 60-70, indicating that these samples have undergone only minor crystal fractionation from primary magmas (Fig. 4a). There is little variation in SiO_2 (55.3–57.9 wt.%) within the sample set. Previous studies of the Diamante-Maipo Caldera (Hickey et al., 1986; Futa and Stern, 1988, Sruoga et al., 2005; Holm et al., 2014) have primarily sampled volcanics with significant europium anomalies ($Eu^* = [Sm_N \times Gd_N]^{0.5}$; Fig. 4b), indicating fractionation of plagioclase or mixing between primitive and evolved magmas (e.g. Turner and Langmuir, 2015a). In contrast, our higher Mg# samples have Eu/Eu*>0.9 (Fig. 4b). Olivine phenocryst compositions range from $Fo_{83.6-75.7}$ at the arc-front, which lie below the olivine-whole rock equilibrium line, indicating that some olivine accumulation has occurred. This demonstrates the importance of utilizing individual mineral analysis in conjunction with whole rock data, as the highest Mg# Maipo lavas (Mg#~70) appear to represent the addition of up to 7wt% olivine to more evolved melts rather than the most "primitive" bulk compositions (Fig. 4a-b; Fig. SB2; Hickey et al., 2016).

Like most arc magmas, mafic Don Casimiro-Maipo lavas have high abundances of Cs, Rb, Ba, U, Th, Pb, and Sr, and depletions in Nb and Ta relative to other elements of similar incompatibility during mantle melting (Fig. 1b). Highly incompatible trace element abundances of these lavas are elevated relative to typical mafic to intermediate samples from oceanic arcs and the SSVZ. Additionally, compared to other primitive SVZ samples, Don Casimiro-Maipo lavas exhibit lower Cs/Rb, smaller Zr-Hf depletions (Hf/Sm~0.9; Fig. SB3), and significantly more enriched isotope ratios (higher $^{87}Sr/^{86}Sr$ and lower $^{143}Nd/^{144}Nd$; Fig. 3b). Finally, the isotopic compositions of the most primitive Don Casimiro samples from this study have lower $^{87}Sr/^{86}Sr$ and higher $^{143}Nd/^{144}Nd$ than Maipo lavas and literature samples from throughout the Diamante-Maipo caldera (Fig. 3b).

Rear-arc scoria samples are basalts-trachybasalts (Fig. 3a; Mg#s of 58–71; assuming $Fe^{3+/}Fe_T$=0.15). Olivine core compositions have higher forsterite contents than Don Casimiro-Maipo samples ($Fo_{90.1–80.6}$ vs. $Fo_{83.6-75.7}$), and lie close to the equilibrium field (Appendix 3; Fig. SB2a). Trace element patterns in the rear-arc show prominent subduction signatures (e.g. Nb-Ta depletion, Pb enrichment, and Th/Nb up to 0.72), and concentrations even higher than Don Casimiro-Maipo lavas (Fig. 1b). As noted by Holm et al. (2016), rear-arc samples have slight depletions in the high field strength elements Zr and Hf, though such depletions are comparable to those observed within the SVZ arc front (Hf/Sm=~0.6; Fig. SB2). $^{87}Sr/^{86}Sr$ and $^{143}Nd/^{144}Nd$ ratios of the new rear-arc samples plot between Don Casimiro-Maipo and literature SVZ data, and are mostly offset from the filtered rear-arc literature data to higher $^{87}Sr/^{86}Sr$ at a given $^{143}Nd/^{144}Nd$ (Fig. 3b).

4. Discussion

The northward increase in crustal thickness in the SVZ theoretically provides the ideal setting to understand the relationship between primitive magma compositions and crustal thickness. However, the scarcity of geochemical data for mafic lavas in the NSVZ has hindered unbiased assessments of the composition of parental magma compositions, and thus the origin of regional geochemical variations. The more primitive nature of Don Casimiro-Maipo samples investigated in this study provide a novel opportunity to re-evaluate the relative contributions from crustal processing, mantle melting, slab fluxes, subduction erosion, and ambient mantle heterogeneity.

4.1. Crustal processing at Don Casimiro-Maipo

Hildreth and Moorbath (1988) suggested that mantle-derived magmas in the SVZ are processed in a melting, assimilation, storage, and homogenization (MASH) zone in the lower crust. In their model, mantle melts throughout the SVZ have similar compositions, and the enriched “baseline” composition of NSVZ magmas results from increased MASH processing in the north, where the crust is thickest. A compilation of samples from the entire Don Casimiro-Maipo caldera (this study and literature) indicates a role for crustal assimilation or mixing during fractional crystallization (AFC) in the petrogenesis of more evolved lavas. For example, the $^{87}Sr/^{86}Sr$ and $^{143}Nd/^{144}Nd$ ratios of Diamante Caldera lavas correlate with MgO and Eu/Eu* (Fig. SB1). These geochemical trajectories can be recreated with a simple model whereby the compositions of sampled crustal lithologies (Lucassen et al. 2001; Lucassen et al., 2004) are mixed in variable proportions with primitive Don Casimiro-Maipo lavas (Fig. 4c-d). The MASH model proposed that the isotopic and trace element enrichment in even the most primitive NSVZ volcanics were caused by crustal assimilation and fractionation of parental magmas that are similar to SSVZ primary magmas. However, the new primitive NSVZ samples, when combined with an SVZ dataset extending from the SSVZ to the NSVZ, clearly demonstrate that the enriched compositions of high Mg# NSVZ lavas cannot be produced by MASH.

To test the MASH hypothesis, the composition of SSVZ volcanics will be represented by an average composition of mafic samples from Villarrica, which erupts high-Mg# lavas and has a similar trace element and isotopic composition to the other volcanoes of the SSVZ (Fig. 1a, Fig. 3b; Turner et al., 2016). As an initial demonstration, the crustal lithologies which recreate the geochemical trajectories *within* the Diamante-Maipo Caldera were mixed with the composition of mafic Villarrica lavas. These mixing trends produce rapidly decreasing K/Rb ratios prior to producing adequate enrichment in $^{87}Sr/^{86}Sr$, and none reach high enough Rb/Y (Fig. 4c-d). Thus, assimilation of these lithologies cannot bridge the compositional gap between the SSVZ and NSVZ.

To test whether *any* plausible Andean crustal assimilant can bridge the compositional gap between the NSVZ (Don Casimiro-Maipo) and SSVZ (Villarrica), the compositions of 348 basement outcrops and basement xenoliths from the SVZ and the surrounding area (22-46°S) were compiled (Lucassen et al. 2001; Lucassen et al., 2004 and others; Appendix 5). As above, assimilation was modelled by mixing the average composition of mafic Villarrica samples with each basement lithology (for mixing proportions between 0–100%). Only 14% of potential assimilants produce mixed compositions within $^{87}Sr/^{86}Sr \pm 0.0001$ and $^{143}Nd/^{144}Nd \pm 0.00005$ of the primitive Don Casimiro-Maipo average (Fig. 5a). Of these isotopically plausible mixed compositions, only 35% have Eu anomalies within the range of the primitive Don Casimiro-Maipo samples (Eu/Eu*>0.9). None of this subset of mixed compositions have trace element signatures resembling Don Casimiro-Maipo (Fig. 5b). Incorporating crystal fractionation alongside these simple assimilation models also cannot account for these compositional offsets, because the resulting compositions produce mismatches not only in overall elemental abundances, but also in a variety of incompatible element ratios that are not fractionated by early-crystallizing phases.

It remains possible that the required MASH assimilant has evaded sampling within the Southern Andes. To address this possibility, we assess the chemical characteristics that a hypothetical assimilant must possess to bridge the compositional gap between the NSVZ and SSVZ. Assuming a maximum of 20% assimilation, based on the relatively high Mg#s of primitive Don Casimiro-Maipo lavas (assimilation drives cooling and crystal fractionation; DePaolo, 1981), any suitable assimilant must have greater than ~450ppm Zr, ~1420ppm Sr, and ~0.63wt% P_2O_5. It is improbable that crustal lithologies will possess these characteristics, because these elements typically become depleted, rather than enriched, during late stage crystal fractionation or crustal melting (Turner and Langmuir, 2015a). To illustrate this point, a compilation of all continental granites, diorites, syenites, and monzonites in the GEOROC database (N~3000 with trace element data) was searched for suitable assimilants (considering only trace element abundances). Only 15 samples (0.5% of the entire compilation) possessed sufficient concentrations of Zr, Sr, and P_2O_5. Mixing of these lithologies with mafic Villarrica lavas produces compositions with erratic trace element patterns, testament to the complex petrological histories of these unusually enriched basement lithologies. None recreate the observed trace element pattern of Don Casimiro-Maipo, particularly the negative Nb-Ta anomaly (Fig. 5c). Thus, although crustal assimilation is common among more evolved samples from the NSVZ, the compositional offset between mafic NSVZ and SSVZ lavas is unlikely to have been generated by assimilation in the lower crust. The failure of the MASH model is most apparent when the full trace element signatures of regional crustal assimilants are considered, along with fundamental considerations regarding the processes causing enriched basement lithologies worldwide.

The geochemistry of rear-arc samples further reinforces the conclusion that the isotopic offsets between NSVZ and SSVZ samples are not produced by MASH. The trace element and isotopic compositions of all the rear-arc samples collected in this study indicate that the rear-arc mantle has been sporadically infiltrated by slab melts. By filtering a compilation of all published data from SVZ rear-arc monogenetic cones to remove samples with large slab additions, it becomes apparent that rear-arc $^{87}Sr/^{86}Sr$ and $^{143}Nd/^{144}Nd$ data plot along the "mantle array" (Fig. 3a; Søager et al., 2013; 2015a-b; Søager and Holm, 2013; Kay et al., 2013; Jacques et al., 2013; 2014; Holm et al., 2014; Turner et al. 2017). This trajectory is not consistent with assimilation of available basement (e.g. Fig. 5b), because highly primitive samples are available at all points along the array. Additionally, unlike the arc-front samples, many of the primitive rear-arc volcanics bear highly forsteritic olivines, nearly in equilibrium with the mantle (Fig. SB2a). It is difficult to reconcile the presence of these primitive olivines with models invoking large amounts of crustal assimilation (e.g. 70% assimilation; Søager et al., 2013), as heat loss during assimilation would drive olivine compositions towards more evolved forsterite contents. Additionally, rear-arc isotopic variability shows similar spatial trends to that observed at the arc-front, despite substantial longitudinal offsets (Fig. 6a-b). Crustal contamination cannot explain this similarity, as accretion and eastward migration of the arc-front since the Palaeozoic has produced a longitudinally fragmented basement, with different basement domains striking parallel to the coast (Kay et al., 2005). Assimilation of lithologies within these different basement domains would be expected to produce uncorrelated rear-arc and arc-front isotope systematics. In contrast, mantle flow paths *are* predicted to travel directly from the rear-arc to arc front, providing a coherent mechanism to account for the synchronized latitudinal changes in arc-front and rear-arc volcanics. In fact, the coincidence of along-strike rear-arc and arc-front geochemical trends is one of the strongest pieces of evidence that the enriched compositions of NSVZ magmas are derived from the mantle rather than the crust. Additional consideration will be given to this observation in section 4.5.

4.2 Assessing the slab and mantle melting contributions to SVZ compositional variation

As with other arcs, variable slab components and mantle melting processes may affect the chemistry of SVZ volcanics. The NSVZ mantle wedge is likely to have a lower maximum extent of melting than the SSVZ, because the thickened over-riding plate in the NSVZ forces high wedge temperatures to greater pressures (Turner et al., 2016). This should lead to enrichment of incompatible elements in the NSVZ (e.g. Tormey et al., 1986; Jacques et al., 2014; Turner et al., 2016). In addition to variability in mantle melt extent (F), the trace element compositions of primary arc magmas are influenced by slab materials. For example, Jacques et al. (2014) attribute compositional variability in the SSVZ to varying slab fluxes. To assess whether the compositional differences between the NSVZ and SSVZ can be accounted for by varying F and/or slab components, it is useful to consider the maximum solution space generated by varying these parameters in tandem.

For this exercise, trace element and isotopic concentrations were calculated using an adapted version of the mantle melting model of Turner and Langmuir (2015a; see SIA4). The compositions of subducted sediment and AOC were taken from the average isotopic and trace element compositions of sediment core ODP1232 (Turner et al., 2017) and NMORB (Gale et al., 2013). As numerical models indicate that SVZ slab top temperatures are well above the wet pelite and AOC solidi (Syracuse et al., 2010; Hermann and Spandler, 2007; Carter et al. 2015; Jacques et al., 2013; 2014), and only hydrous melt (as opposed to aqueous fluid) eclogite partition coefficients produce successful models of trace element abundances (Turner et al., 2017), it was assumed that slab melts (rather than fluids) were added to the mantle wedge. Slab melt compositions were calculated using the aggregate fractional melting equation and partition coefficients consistent with experiments (SIA4.1; Kessel et al., 2005; Hermann and Rubatto, 2009; Skora and Blundy, 2010). Slab melts were then mixed with a depleted upper mantle composition assigned the trace element abundances of Workman and Hart (2005), and the isotopic composition of the rear-arc sample 126171 (Baseline Andean Mantle (BAM); Figs 3a, 6a-b; Søager et al., 2013). This isotopic composition defines the low Sr and high Nd end-member of the rear-arc array (Fig. 3a) and has a trace element composition that appears free of slab material (e.g. Th/Nb<0.06, Ce/Pb>25). Finally, the composition of mantle melts were estimated using the batch melting equation, with experimentally-derived hydrous peridotite partition coefficients and melt reaction coefficients (model details in SIA4.1).

Firstly, we consider the solution space for $^{87}Sr/^{86}Sr$ vs. $^{143}Nd/^{144}Nd$, which is simplified by the fact that these trajectories are not noticeably fractionated by variations in slab temperature, and are insensitive to varying melt extents. The pink field on Fig. 7a shows the solution space produced by variations in slab temperature and the proportions of slab melts. The isotopic composition of Villarrica (and most SSVZ) volcanics is encompassed within this field. However, TSVZ and Don Casimiro samples plot significantly below this field. As variable slab contributions predominantly drive wedge compositions to higher ^{87}Sr/^{86}Sr at near constant or increasing ^{143}Nd/^{144}Nd, another process is clearly needed to recreate the low ^{143}Nd/^{144}Nd ratios in TSVZ and NSVZ volcanics.

A similar solution space for trace element ratios is shown in Fig. 7b. The pink area encompasses the space made available by varying the proportions of a slab melts (with slab melting at ~800 C) and F within reasonable bounds. F=0.04 was chosen as the lowest plausible mantle melting extent because F values <0.04 tend to produce alkali-basalt or silica-undersaturated major element compositions (e.g. Baasner et al., 2016). Villarrica samples plot within this field, and a model fit can be found that reproduces the entire suite of Villarrica incompatible trace elements and radiogenic isotope ratios (Figs. 7-8). While this model fit does not represent a unique solution for Villarrica, it does demonstrate that a feasible quantitative solution exists that is consistent with available experimental constraints. As in Fig. 7a, the compositions of most TSVZ and Don Casimiro-Maipo lavas fall outside of this solution space. The addition of sediment and AOC melt to the depleted mantle source can generate high La/Sm, but only at excessively high Sr/Nd (Fig. 7a). While reducing F can increase La/Sm, even at F=0.04 there is no plausible trace element match to the Don Casimiro-Maipo lavas within this parameter space.

Slab temperatures might also affect the trace element compositions of SVZ volcanics. There are systematic changes in the slab age and depth beneath the SVZ arc front, both of which may lead to variability in the temperature of the slab surface beneath the arc front (Syracuse et al., 2010). Certain aspects of the trace element differences between Don Casimiro-Maipo and Villarrica are indeed suggestive of slab temperature variations. Compared to Villarrica, Don Casimiro-Maipo has low Cs/Rb and high Hf/Sm ratios (Fig. 1b). These element ratios are not substantially fractionated from each other during melting, and may indicate higher slab temperatures in the NSVZ. For example, Cs is highly mobile in low temperature aqueous fluids, and may have been disproportionally lost during early slab dehydration in the NSVZ, where the sub-arc slab is deeper (Savov et al., 2007; Spandler et al., 2007). Additionally, a hotter slab temperature can destabilize zircon during slab melting, which may lead to the less pronounced Zr-Hf depletions at Don Casimiro-Maipo (e.g. Hirai et al., 2018). The blue field on Fig. 7b shows the expansion of the solution space for slab temperatures hotter than 900˚C (calculated using the maximum measured experimental mobility of light rare earth elements in slab melts; see SIA4.1). While the solution space at very high slab temperatures may shift toward higher La/Sm ratios at a given Sr/Nd ratio, the mafic NSVZ volcanic rocks remain well outside of the realm of possible solutions. Overall, the trace element and isotopic differences between mafic SSVZ and NSVZ volcanics cannot be recreated by variable slab additions and melt extents, even in combination. This indicates that the sub-arc mantle within the SVZ must be variably enriched to account for the prominent latitudinal variations in geochemistry.

4.3 Is there geochemical evidence for subduction erosion?

SVZ rear-arc volcanics form a linear array between MORB-like compositions and EM1-type OIBs in ^{87}Sr/^{86}Sr vs. ^{143}Nd/^{144}Nd space (Kay et al., 2013; Søager et al., 2015a; Fig. 3a), and both rear-arc and arc-front samples are characterized by similar along-strike variability in these isotope ratios (Fig. 6a-b). As the isotopic offset between the mafic NSVZ and SSVZ samples is inconsistent with crustal assimilation or variable slab additions, an alternative mechanism is required to introduce an EM1-like contaminant to the mantle source of the SVZ.

The origins of EM1-type OIBs are debated, with suggestions including deep recycling of lower continental crust (LCC), pelagic sediment and oceanic crust, or metasomatized subcontinental lithospheric mantle (Willbold and Stracke, 2010). The first suggestion is particularly apt, as it has been argued that the NSVZ endured extensive subduction erosion (the removal of upper plate material via abrasion and plucking by the lower plate) throughout the Cenozoic (Stern, 1989; Stern, 2011). Although the composition of the Andean LCC is not well constrained, an extensive compilation of regional basement compositions (Appendix 5) constrains the compositional range of this reservoir. While these samples were collected from surface outcrops, Miocene episodes of tectonic thickening and under-thrusting have resulted in similar lithologies residing at deeper levels in the crust (Hildreth and Moorbath, 1991). Hence, this compilation can be used to assess the subduction erosion hypothesis, regardless of whether the UCC, LCC or the entire crustal column (Holm et al., 2014; 2016) on the leading edge of the South American plate undergoes recycling.

We assess the ability of subduction erosion to reproduce along-arc geochemical trends by mixing the composition of basement lithologies (Appendix 5) into the estimated composition of the metasomatized Villarrica mantle source. Melts of the resulting mixes were calculated using the model described above at melt generation conditions indicated by thermal models for Don Casimiro-Maipo (F=0.056, P=33kbar; Turner et al., 2016). Only 11% of the mixed compositions pass within ^{87}Sr/^{86}Sr±0.0001 and ^{143}Nd/^{144}Nd±0.00005 of the most primitive Don Casimiro-Maipo samples (Fig. 9a). Only 15% of these isotopically plausible mixed compositions have Eu anomalies within the range of the primitive Don Casimiro-Maipo samples (Eu/Eu*>0.9), none of which recreate the concentrations of Y, Gd, Sm, Sr, Ba and ^{87}Sr/^{86}Sr ratios (Fig. 9b-c). This analysis demonstrates that no mixed composition with adequate trace element data plots within the range of the Don Casimiro-Maipo for ^{87}Sr/^{86}Sr, ^{143}Nd/^{144}Nd, and trace element abundances.

While some previous studies of the NSVZ (e.g. Holm et al., 2014; 2016) have concluded that eroded continental material is the most plausible candidate for the enriched mantle end-member in this region, our analysis does not support this conclusion. This discrepancy results from the more primitive nature of the newly sampled Don Casimiro-Maipo samples. The low Eu/Eu* ratios seen in samples from other studies may well result from plagioclase fractionation, magma mixing, or crustal assimilation, implying that this signature is a secondary overprint, rather than a source characteristic.

As with crustal assimilation during magmatic ascent, it is possible that the appropriate eroded crustal lithology has avoided sampling due to the restricted basement exposure in the SVZ. However, regional considerations indicate that LCC recycling is unlikely to produce the observed EM1-like enrichment. Willbold and Stracke (2010) present a model in which EM1-like isotopic compositions are produced by mixing LCC starting materials into normal MORB mantle. However, this model assumes that the recycled LCC domains have been extracted and isolated from the mantle for >4 Ga, while the Chilenia and Cuyania terranes comprising the lower crust of the NSVZ-TSVZ are only of Grenvillian age (~1Ga; Ramos, 2010). This relatively young age causes typical Southern Andean basement to have ^{187}Sr/^{86}Sr ratios that are too high (relative to ^{143}Nd/^{144}Nd) to serve as an appropriate end-member (see mixed compositions in Fig. 9a).

Rear-arc geochemical variability is also inconsistent with the subduction erosion hypothesis, because rear-arc isotopic enrichment persists at distances exceeding 600 km from the trench. It is unlikely that material eroded at the trench could spread hundreds of kilometres towards the rear arc, in the opposite direction of corner flow (MacDougall et al., 2017). While eroded material may instead be carried down with the subducting slab and released alongside other slab inputs, in this case the enriched signature would co-vary with other slab components. Instead, at 550 km from the trench, rear-arc monogenetic samples have Ce/Pb ratios that range from 5 (similar to the arc front) to >20 (similar to MORBs; Fig. 10b), but retain $^{143}Nd/^{144}Nd$ ratios that are consistently enriched relative to DMM (Fig. 3a). Additionally, within a given latitude bracket, rear-arc $^{143}Nd/^{144}Nd$ ratios have limited variability, and do not correlate significantly with Ce/Pb or other indices of slab additions. Finally, isotopic enrichment in both the rear arc and arc front increases in a reasonably symmetrical, coherent fashion on either side of a pronounced minima at 39° S (Fig. 6a-b; Turner et al., 2017). Although it has been suggested that subduction erosion increases northwards (Stern, 1989), this phenomenon cannot account for the increase in enrichment south of Villarrica. The spatial systematics of rear-arc compositions are therefore also inconsistent with subduction erosion.

Overall, when the full array of trace element abundances and isotopic ratios are considered, subduction erosion cannot recreate the notable geochemical trends in rear-arc and arc-front data. This may indicate that the extent of subduction erosion has been over-estimated for this region. Erosion rates are calculated based on the assumption that the distance between the trench and the arc front remained constant throughout the Miocene (Stern, 1989). However, more recent geophysical models find that arc-front migration relative to trench location might be a common process (e.g. Karlstrom et al., 2014). The suggestion that the locus of subduction-related volcanism has shifted during this same period as a function of varying slab angle also undermines a direct connection between subduction erosion and arc-front location. Alternatively, it is possible that subduction erosion did indeed influence the mantle wedge composition at some point in the Miocene, but corner flow towards the arc has since flushed the present-day mantle wedge of eroded material. Regardless of the explanation, the plausible geochemical impacts of subduction erosion are inconsistent with the along-strike enrichment trend of the SVZ. Clearly some other mechanism is required to explain SVZ geochemical variability.

4.4 EM1-type enrichment from a sub-continental lithospheric mantle source

An alternative source for the enriched EM1-like mantle signature of the NSVZ is the recycling of Metasomatised Subcontinental Lithospheric Mantle (M-SCLM). The infiltration of low degree mantle melts (F~0.005) into the base of the lithospheric mantle produces enriched incompatible element concentrations, which rapidly evolve EM1-like isotopic compositions (McKenzie and O'Nions, 1995; Turner et al., 2017; Fig. 11). Unlike crustally-derived materials, M-SCLM provides a more homogenous end-member composition that is capable of recreating the remarkably coherent geochemical trends observed in the SVZ (Rogers and Hawkesworth, 1989; Turner et al, 2017). M-SCLM material may be stored for long periods in the lithospheric mantle until it is returned to the asthenosphere by delamination or erosion driven by corner flow.

Field evidence supports the hypothesis that the SCLM surrounding the SVZ has EM1-like isotopic affinities. Three geographically separated suites of isotopically enriched igneous rocks across South America have been interpreted as direct melts of the enriched SCLM (see Fig. 2a):

1) Alkaline igneous rocks erupted near the edges of the Rio Apa-Luis Alves and Sao Franscisco Cratons (Gibson et al., 1995; 2005; Carlson et al., 1996).
2) Mesozoic metabasites from the Southern Rift (Lucassen et al., 2002).
3) Carboniferous granitoids from the Santo Domingo Complex of the Coastal Batholith (Parada et al., 1999).

The $^{87}Sr/^{86}Sr$ and $^{143}Nd/^{144}Nd$ of samples from these regions plot as a linear extension of the SVZ rear-arc array (Fig. 11) and cannot be accounted for by addition of variable slab components or assimilation of available basement. The remarkable alignment of these lithologies in isotopic space, despite being geographically separated by hundreds to thousands of kilometres, suggests that M-SCLM east and north of the SVZ has relatively homogeneous EM1 affinities. The isotopic trajectory of these SCLM melts is consistent with the expected isotopic evolution of SCLM enriched by low degree mantle melts (Turner et al., 2017; Fig. 11). In contrast, the field produced by addition of sampled basement lithologies to the mantle has higher $^{87}Sr/^{86}Sr$ at a given $^{143}Nd/^{144}Nd$ than the array of SCLM-melts and rear-arc volcanics, and a significantly broader trajectory (grey field, Fig. 11).

Rather than attempt to estimate the full trace element composition of very low-degree metasomatising mantle melts, a proxy for the composition of mantle domains which has been enriched by M-SCLM melts was estimated by inverting for the mantle source composition of Gough Island EM1-type OIB volcanics (Turner et al., 2017), where enrichment has been specifically linked to deep recycling of SCLM (Gibson et al., 2005; Boyet et al., 2019). Trace element and isotopic ratios of the inverted source composition were subsequently adjusted within the limits of EM1-like ocean island basalts (Stracke et al. 2003; Willbold and Stracke, 2010) to produce a generic EM1 source (SIA4.2). Including EM1-like mantle heterogeneity as an additional parameter sufficiently expands the solution spaces on Fig. 7a-b (grey fields) to overlap the composition of primitive Don Casimiro-Maipo lavas. Furthermore, a model fit incorporating this EM1-type mantle component recreates the isotopic composition and entire suite of incompatible trace element concentrations at Don Casimiro-Maipo (Fig. 7–8). As with the model fit for Villarrica, this does not represent a unique solution, but does demonstrate that the observed geochemical enrichment at Don Casimiro-Maipo is quantitatively consistent with all available constraints, unlike models relying upon MASH, LCC recycling, or variable slab components.

The addition of M-SCLM to the mantle by erosion or delamination at the base of continental cratons behind the volcanic arc also accounts for the spatial variability in rear-arc and arc-front geochemistry. Turner et al. (2017) proposed two explanations for the gradual decline in isotopic enrichment towards a distinct minimum at 39°S (Fig. 6a-b). Firstly, they note the presence of a Permian terrane suture at 39° S (Rapalini et al., 2010). It is possible that M-SCLM was lost during rifting or subsequent collision between cratonic blocks (Fig. 12a). Secondly, a vertical and horizontal slab tear has been inferred based on seismic imaging at ~39° S, (Pesicek et al., 2012). If M-SCLM is entrained equally throughout the SVZ, upwelling of depleted Pacific mantle (which has not interacted with M-SCLM) through these features could dilute the EM1 signature. The upwelling, depleted mantle would then spread northwards and southwards, perhaps aided by toroidal flow (Zandt and Humphreys, 2008), resulting in a gradual northward and southward increase in enrichment (Fig. 12b). This upwelling material could also produce the magnetotellurically imaged "plume" in the rear-arc (Burd et al., 2014). Geochemical signatures associated with upwelling through a slab window in the Kula Volcanic Field (W. Anatolia, Turkey) are traced over >250km (Klaver et al., 2016), similar to the distances observed here.

4.5 A unified model for the SVZ arc-front and rear-arc

The preceding sections have shown that the first-order geochemical variability in the SVZ arc-front and rear-arc is consistent with the mixing of EM1-type and isotopically depleted mantle end-members. This is similar to the proposal of Jacques et al. (2013, 2014), though by including the influence of ambient mantle enrichment on trace element abundances, our model does not require substantial variations in the composition of slab components, or exceedingly low extents of melting to account for arc-front compositions. In contrast to these unified models of arc-front and rear-arc geochemistry, other models calling upon unique processes specific to particular regions of the rear-arc have been proposed. For example, Søager et al. (2015a; b) invoke the presence of a distinct mantle component that is specific to Southern Payenia, Søager et al. (2013, 2015a) propose that rear-arc magmas have assimilated up to 70% LCC to accommodate certain trace element ratio trajectories in basalts from the Nevado volcanic field (~35-36˚S), and Holm et al. (2016) invoke enriched mantle and eroded crust to account for the geochemical variation observed in the Northern Segment of the rear-arc (~34-35 ˚S). To assess whether these region-specific observations can be accounted for by our unified model, it is important to consider the detailed characteristics of across-arc geochemical trends and the influence of temporal variability in SVZ subduction geometry.

The extent to which slab materials have infiltrated the rear-arc mantle can be investigated using trace element ratios sensitive to the addition of slab melts (e.g. Th/Nb, Th/La, and Ce/Pb; Johnson and Plank, 1999; Plank, 2005; Fig. 10a). Remarkably, while these slab-sensitive ratios generally show declining slab fluxes with increasing trench distance, some cones retain elevated Th/La and Th/Nb, and low Ce/Pb at nearly 600km from the trench (Fig. 10b). Variations in slab temperature should significantly fractionate these ratios. If across-arc slab temperature variations are in accord with thermal models (Syracuse et al., 2010), then Th/La in slab melts may increase by ~25% from the arc-front to the rear-arc, and Th/Nb by nearly an order of magnitude (Hermann and Rubatto, 2009). This variability in the composition of slab melts should result in rear-arc and arc-front lavas following distinct mixing trajectories. Yet, all rear-arc samples lie on mixing lines between the modelled arc-front slab melt composition (e.g. Fig. 8) and an ambient mantle with varying amounts of EM1-like enrichment (Fig. 10a). The high slab temperatures beneath rear-arc cones should also destabilize zircon (e.g. Harai et al., 2018). However, rear-arc samples have Zr-Hf anomalies similar to TSVZ and SSVZ arc-front volcanoes (Fig. SB3). These observations imply that the slab components reaching the rear-arc and arc-front mantle sources were extracted from the slab at similar temperatures.

It is possible that the signal of relatively cold slab melts beneath the rear arc is a remnant from a period of shallow subduction, and not related to the present-day slab geometry (Søager et al., 2013), though it is difficult to reconcile the chronology of such a process. In Southern Payenia, it is generally accepted that the slab steepened towards its current configuration at ~5 Ma (Kay et al., 2005). However, Gudnanson et al. (2012) attribute the northward propagation of quaternary rear-arc volcanism to a significant delay in slab rollback in this region, while Folguera et al. (2009) suggest that the recent volcanism behind the NSVZ is instead due to extension collapse. In considering these competing theories, an essential observation is that volcanism within the Diamante-Maipo caldera has been essentially uninterrupted since the Late Miocene (Sruoga et al., 2005). This indicates that the NSVZ slab geometry is unlikely to have shifted substantially over the past 5 Ma. To date, no physical model of late slab steepening has been proposed which satisfies observations from both the arc-front and rear-arc. Because the rear-arc samples of this study were likely erupted between 0.01–0.7 Ma (Folguera et al., 2009), corner flow over the 4-5 Myrs following slab steepening should have led to ~330 km of wedge turnover prior to their eruption, effectively flushing any Miocene slab inputs from the rear-arc asthenosphere.

Thus, the slab component observed in northern rear-arc cones was likely derived from the slab in its current geometry, and some other mechanism is required to account for the uniform across-arc slab-component compositions. The results of two-phase thermo-mechanical models provide an explanation for this phenomenon. The mantle source at the arc front is likely influenced by slab materials that have been extracted from the slab well beyond the arc front, and then deflected towards the trench along compaction pressure gradients (Wilson et al., 2014). The rear-arc asthenosphere is plausibly influenced by slab melts extracted at shallower depths and then transported away from the trench in zones of low porosity (Cerpa et al., 2017; Fig. 14b). It also is possible that slab materials could be transported non-vertically by "mélange diapirs". However, Cruz-Uribe et al. (2018) found that melts of such diapirs have >50 wt. % SiO_2, >18 wt. % Al_2O_3, and <8 wt. % MgO, while the most primitive SVZ rear-arc basalts have >10 wt. % MgO, <48 wt. % SiO_2, and <15 wt. % Al_2O_3, as is typical of arc alkali basalts generated by low degrees of melting from a lherzolite source (e.g. Baasner et al., 2016). The experimental melts also have positive Zr-Hf anomalies, unlike the negative Zr-Hf anomalies of SVZ rear-arc lavas (Fig. 1b). Overall, the geochemical systematics of SVZ rear-arc volcanics appear to be most consistent with a strong role for slab melting followed by advective transport, compaction channelling, and generally non-vertical transport of slab-derived materials through the wedge, which is broadly consistent with numerical models of two-phase flow (Cagnioncle et al., 2007; Wilson et al., 2014; Cerpa et al., 2017).

Given the general viability of the unified SVZ model of ambient mantle, slab, and melting variation for both the rear-arc and arc front, it is worthwhile to assess whether this model can also account for the observations that motivate region-specific models. Here, we limit this discussion to trends (Figure 13b-d) that have been interpreted as evidence for extensive lower crustal assimilation (up to 70%; Søager et al., 2013; Søager et al., 2015a). While rear-arc compositions on these plots appear to trend toward the compositions of certain lower crustal xenoliths (Kay et al., 1996), calculated mixing lines with these xenoliths are strongly hyperbolic, and deviate substantially from the actual rear-arc compositions (Figure SB5). "Adjusted" lower crust compositions have been proposed to mediate such discrepancies (Søager et al., 2013), though the resulting compositions resemble neither generic models of the LCC (e.g. Rudnick and Gao, 2003), nor the actual compositions of Andean basement samples (Figure SB6). These observations, along with the general difficulty of maintaining high Mg# bulk compositions while enduring such large amounts of crustal assimilation, motivate a re-examination of the assimilation model in particular.

Our analysis suggests that the regional systematics identified by Søager et al. can be fully accounted for by the variations expected from slab fluxes, mantle melting extents, and the ambient mantle. On Figure 13c, both axes are controlled by mantle and slab components, while the y-axis (La/Sm) is also affected by variations in F. The arc-front volcanics have a relatively uniform slab contribution, so follow a trajectory determined by F and the ambient mantle (e.g. Turner et al., 2017). Many of the rear-arc samples overlap the arc-front data, but when slab additions are diminished, the extent of mantle melting often drops to very low values (Jacques et al., 2013), which drives up La/Sm. This is apparent, from the similarly high La/Sm compositions of basalts from the Gough Island chain, which are also alkali basalts produced by low-F melting. Similar systematics can account for variability on Figure 13d, though the divergence between arc-front and rear-arc compositions is less apparent here, as both low-F melt generation and bulk slab additions skew compositions similarly, toward very high Th/Sm. Thus, the variability on both 13c and 13d are easily accommodated without a crustal assimilant.

Unlike Th/Sm and La/Sm, the highly-incompatible element ratios on Figure 13b are less affected by variations in melt extent, and can be accounted for by variations in slab flux and mantle enrichment alone. Ba/Th is particularly sensitive to small variations in the compositions of subducting slab materials and temperatures of slab melting (e.g. Carter et al., 2015; Patino et al., 2000). This is evident from the high Ba/Th mafic enclaves erupted at Longavi Volcano, which are thought to be representative of parental magmas (Rodriguez et al., 2007). Rodriguez et al. demonstrate that these lavas reflect input of a particularly high Ba/Th slab component to the mantle, and suggest this is caused by the proximal subduction of the Mocho

Fracture Zone (Figure 13a). Hydrothermal alteration, which was likely enhanced along the fracture zone, produces elevated Ba abundances in both ocean crust and sediment (Kelley et al., 2003; Plank et al., 2013). Alternatively, the fracture zone may introduce an additional high-Ba fluid component to the wedge. Subducting fracture zones have inevitably swept along the arc over time, causing transient geochemical impacts of such extremely sensitive slab tracers in local volcanics (Figure 13a). Given the large range in the Ba/Th ratio of the slab component, there is no need to invoke extremely large quantities of lower crustal assimilation (>70%) to account for the regional systematics. While geochemical variability, when considered on a small enough scale, necessarily requires case-specific ad-hoc modelling, the regional trends of the SVZ appear consistent with the relatively simple three parameter model developed here, which incorporates processes seen in subduction zones worldwide.

5. Conclusions

The origin of trace element and isotopic enrichment in thick-crusted continental arcs has profound implications for the formation of the continental crust and the petrogenesis of evolved magmas. The new high Mg# samples characterized here provide valuable new constraints on the compositions of parental magmas from the thick-crusted northern SVZ (NSVZ). These new analyses demonstrate that while evolved NSVZ underwent crustal assimilation during fractional crystallization, the geochemical offsets between the most primitive Southern SVZ (SSVZ) and NSVZ volcanics cannot be produced assimilation of any basement lithologies either within the Southern Andes, or globally. Similarly, while variations in the extent of mantle melting and subtle differences in slab additions may arise due to the thicker lithosphere and deeper slab in the NSVZ, the solution space made available by these parameters does not encompass the trace element or isotopic compositions of mafic Don-Casimiro Maipo samples. Only models incorporating an enriched ambient mantle domain that is compositionally similar to the mantle source of EM1-type OIBs can recreate the observed isotopic and trace element enrichment in mafic samples from Don Casimiro-Maipo. Coincident arc-front and rear-arc regional variations in isotopic enrichment indicate that this signal arises from the ambient mantle. A forward model based on an inversion for an EM1-like mantle source successfully reproduces the isotopic composition and trace element composition of Don-Casimiro Maipo, demonstrating that this interpretation is consistent with available experimental constraints.

The SVZ EM1 component is most plausibly generated by melt-metasomatism of sub-continental lithospheric mantle, which is eventually returned to the asthenosphere by erosion at the base of cratonic blocks, transported trench-ward by corner flow. An alternative scenario in which the EM1 signal results from subduction erosion of continental material produces unsuitable isotopic systematics and erratic trace element patterns. Additionally, the coherent latitudinal variations observed in arc-front and rear-arc lavas are difficult to reconcile with subduction erosion of fragmented basement domains.

The isotopic trajectory of the rear-arc lavas is co-linear with other South American lavas that are thought to be melts of metasomatized sub-continental lithospheric mantle (M-SCLM). This supports a model in which the enriched mantle source is derived from the addition of M-SCLM material to the mantle wedge by erosion or delamination from the cratonic lithosphere behind the arc. Unlike the longitudinally fragmented and highly heterogeneous Andean basement, the composition of the M-SCLM appears to be relatively homogenous across a large area of South America. Thus, unlike subduction erosion or crustal assimilation, variable mantle enrichment due to mixing of an EM1-like NSVZ mantle source with a depleted mantle component can account for along and across-arc geochemical variations. In addition to chemical variability induced by variable M-SCLM addition, rear-arc cones receive highly variable slab inputs that are surprisingly similar in composition to the arc front. This, along with variable melt extents, accounts for the offset trajectories of rear-arc and arc-front lavas, and provides support for recent two-phase flow models indicating non-vertical transport of slab materials (Cagnioncle et al., 2007; Wilson et al., 2014; Cerpa et al., 2017).

Overall, we demonstrate that the enriched trace element and isotopic compositions of primitive lavas in the thick-crusted NSVZ are produced by low-degree melting of an enriched ambient mantle that is metasomatized by slab melts (Turner et al., 2017), rather than crystal fractionation and crustal assimilation. The similarities between the trace element signatures of primitive NSVZ lavas and the bulk continental crust (Fig. 1) implies that ambient mantle enrichments may play a major role in the origin of enriched continental compositions globally. Revaluation of enriched signatures in primitive lavas of other thick-crusted arcs (e.g. Cascades, Mexico, Guatemala, Colombia) will allow assessment of the global importance of ambient mantle enrichment. If similarities with the SVZ are found, models of continental crust generation and elemental cycling within the silicate earth will require re-evaluation.

Acknowledgments

The authors acknowledge NERC grant ‘Mantle volatiles: processes, reservoirs and fluxes’ (NE/M000427/1) for funding, Melissa Murphy for help with clean lab chemistry, Sally Gibson for use of the LA-ICP-MS, Jason Day for helping with analysis, and Patrick Sugden for assistance with sample preparation for Sr and Nd isotopes in Leeds.

Figure Captions

Fig. 1– Incompatible trace element “spider diagrams”, normalized to D-MORB (Gale et al., 2013). a) Literature data for Don Casimiro-Maipo (Hickey et al., 1986) has incompatible trace element abundances comparable to bulk continental crust (Rudnick and Gao, 2003) and the Northern Cascades (Mt Ranier - Sisson et al., 2014; Mt Hood; Baggerman et al. 2011). Don Casimiro-Maipo shows significantly more enriched trace element abundances than the TSVZ, SSVZ, and the majority of island arcs (GEOROC compilation). Villarrica, which has a similar trace element signature to other SSVZ centres (Llaima, Puyehue and Osorno shown here; Turner et al. 2016), is used as a representative SSVZ end-member in figures 3, 4, 6, 8 and 9. b) Trace element data collected in this study for 7 rear-arc cones, and the most primitive samples from Don Casimiro-Maipo. The observed HREE depletion in Don Casimiro-Maipo samples indicates the presence of residual garnet during mantle melting. Rear-arc samples show distinctive arc-like signatures, and even greater trace element enrichment than Don Casimiro-Maipo samples.

Fig. 2-Geographical context and sample locations. a) Map of the SVZ, showing the segment boundaries defined by Dungan et al. (2001). The locations of arc-front and rear-arc samples of this study are shown, along with the locations of arc-front volcanoes passing the filters of Turner et al. (2016). The geographical regions containing inferred M-SCLM melts (see Fig. 11) are overlain. Base map from GEOMAP APP. b) Sample locations of Don Casimiro and Basal Maipo lavas within the Diamante-Maipo Caldera Complex. Imagery from Google Earth. c) Moho depth (from the model of Tassara and Echaurren, 2012) vs. volcano latitudes

projected along the vector of convergence to the trench. d-e) Incompatible major and trace element 6-vaues (Turner et al. 2016, and this study) increase northwards, mirroring changes in crustal thickness.

Fig. 3- a) SVZ rear-arc samples which are not dominated by slab inputs (Th/Nb<0.4) plot along the "mantle array", between DMM and EM1-type ocean island basalts. They greatly extend the isotopic range observed among average rear-arc compositions from other arcs (black dots; Turner et al., 2017). Literature values from Don Casimiro-Maipo lie at the enriched end of the global rear-arc array (Hickey et al., 1986). The pink and blue fields envelop all EM1 and EM2-type ocean island basalts from Stracke et al. (2003). The enriched isotopic end-member used for quantitative modelling is taken from Pitcairn (57DS9; Stracke et al., 2003). The Baseline Andean Mantle (BAM) isotopic end member is taken from an SVZ rear-arc sample with no trace of a slab contribution (e.g. Th/Nb<0.06, Ce/Pb>25; Søager et al., 2013; sample 126171). The Nazca Plate sediment composition is the average of ODP1232 (Turner et al., 2017). b) Don Casimiro and Maipo and rear-arc data from this study, alongside literature data from Villarrica and the SVZ that pass filters indicating they are not substantially affected by crustal contamination or mixing (Turner et al., 2016). The filtered rear-arc samples shown in a) are also plotted, along with unfiltered data from the entire Diamante Caldera.

Fig. 4- a) Don Casimiro-Maipo samples from this study are high Mg# basaltic andesites. Circled samples have major element characteristics consistent with olivine accumulation (Fig. SB2). Rear-arc samples are primitive basalts-trachybasalts. Mg#s were calculated assuming $Fe^{3+}/Fe_T = 0.3$ for the arc-front (Holm et al., 2016), and $Fe^{3+}/Fe_T = 0.15$-0.3 for the rear-arc (Søager et al., 2015b, cyan and blue triangles respectively). b) Eu anomalies are negligible in the most primitive samples of this study (>0.9), whereas the majority of literature samples show substantial negative Eu anomalies. Eu/Eu* was calculated with $Eu^* = (Sm_N \times Gd_N)^{0.5}$ or with $Eu^{**} = (Sm_N^2 \times Tb_N)^{1/3}$ where no Gd data was reported. In both cases, element concentrations were normalized to CI chondrite (McDonough and Sun, 1995). c-d) Mixing arrays between eight SVZ basement samples and primitive Don Casimiro-Maipo samples encompass the chemical diversity within the Diamante Caldera (from Lucassen et al. 2001; 84-31-1, 84-31-2, 84-42-1, 84-42-11, and Lucassen et al. 2004; 00-77, 00-55, 00-58 and 00-05). However, mixing between the same 8 samples and Villarrica (grey lines) do not pass through Don Casimiro-Maipo. Models originate from the primitive average of Don Casimiro-Maipo and Villarrica samples. Error bars in c) show ± 1σ of the variation among primitive samples.

Fig. 5-Crustal assimilation models. a) Mixing lines produced between 348 crustal lithologies thought to be representative of SVZ basement (compiled from GEOROC and other sources) and the average composition of primitive Villarrica samples. Only a small proportion pass near Don Casimiro-Maipo. b) Trace element patterns of mixed compositions that have isotopic ratios close to Don Casimiro-Maipo (red lines in a), as well as Eu/Eu*>0.9. Mixtures providing a reasonable match to the La-Ce concentrations (cyan lines) have trace element patterns that are completely distinct from that of Don Casimiro-Maipo. c) Mixed compositions for the small subset of the ~3000 plutonic rocks from GEOROC that have sufficient concentrations of Zr, Sr and P_2O_5 to recreate the enrichment of these elements at Don Casimiro-Maipo via assimilation. Mixed compositions were calculated for the % mixing required to recreate Zr concentrations. All produce erratic trace element patterns that are dissimilar to those observed at Don Casimiro-Maipo.

Fig. 6 - Across and along-arc variation in rear-arc isotopes. a-b) Rear-arc isotopic ratios form latitudinally coherent trends, with statistically significant trend lines ($p<0.005$). A pronounced minimum in $^{87}Sr/^{86}Sr$, and a maximum in $^{143}Nd/^{144}Nd$ is observed at ~39° S, with a reasonably linear and symmetric decrease to the north and south that can be explained by variable EM1 enrichment (pink arrows). Scatter about this first order

trends within the rear-arc results from variable slab fluxes. The blue bar shows the bulk slab compositions for a mix of 20% sediment melt, 80% AOC melt, incorporating the ± 1σ variation of the sediment composition from ODP1232 (Turner et al., 2017). Rear-arc samples from this study fit within the regional trends. Arc-front centres lie close to the rear-arc best fit line, showing that these spatial trends in enrichment are also present at the arc-front. The deviation in ^{143}Nd/^{144}Nd between the rear-arc and the arc-front south of 39° S likely results from the sparse sampling of rear-arc centres, making it difficult to resolve regional trends from local variations in heterogeneity. This difference may also reflect much smaller slab input to the rear-arc than arc-front

Fig. 7 – Trace element and isotopic solution space produced by varying the composition of slab melts, the extent of melting, and the composition of the ambient mantle. a) The pink field represents the maximum isotopic solution space available by the addition of varying slab melt compositions (up to 2% sediment melt, 10% AOC melt) to a depleted mantle (“baseline ambient mantle”; BAM), with a trace element composition of DMM, and isotopic composition of Sample 126171 (Søager et al., 2013). Variable slab temperatures have very little effect on the size of this isotopic solution space, so are not shown. The grey field represents the additional solution space made available by the addition of an EM1-type mantle domain to the composition of the baseline Andean mantle (BAM). b) The pink field represents the maximum solution space available by varying slab additions as in a), in addition to variations in F between 0.04 and 0.3. The teal field represents the additional solution space made available by an increase in slab temperature (with a change in the partition coefficients of La, Sm, and Nd; see SIA4.1). as in a), the grey field represents variable enrichment by an EM1-type mantle source. In both figures, it is clear that only the addition of an EM1-type mantle source to the sub-arc mantle can recreate the composition at Don Casimiro-Maipo. The diamonds represent the best model fits for Villarrica (F=0.1, 7.5% slab addition consisting of 17% sediment, with no enrichment) and Don Casimiro-Maipo (F=0.056, 7.5% slab addition consisting of 23% sediment, with 80% EM1 enrichment). The full trace element signatures of these models are shown in Fig. 8.

Fig. 8 – Trace element modelling results. The trace element composition of Villarrica can be well matched at F=0.1 with addition of 7.5% slab melt consisting of 17% sediment. The extreme trace element enrichment at Don Casimiro-Maipo is best recreated by addition of 80% enriched source, and slight changes in the composition of the slab addition (23% AOC vs. 17% at Villarrica). The mantle melting model includes a parameterization for changing garnet proportions based on melt depths (Gt=0.0067*GPa+0.0017); we assume that melting at Don Casimiro-Maipo and Villarrica occurs at 3.3 GPa and 2.2 GPa respectively (Turner et al., 2016). The solid black lines in both figures represents the best model fit for each centre at the enrichment and proportions of AOC:SED mentioned above using low temperature slab partition coefficients. This provides the best match for Villarrica. The dashed grey lines represent the model fit for each centre at increased slab temperatures, assuming 70% loss of Cs in the forearc. This provides the best model fit for Don Casimiro-Maipo. Model envelopes are produced by adding and subtracting 1σ of 33 measurements of ODP1232 (Turner et al., 2017). Melting conditions were generated directly from the physical modelling results of Turner et al. (2016).

Fig. 9– Modelling contamination of the mantle source by subduction erosion. a) Isotope systematics of contamination of the Villarrica mantle source by subduction erosion. The isotopic composition of the Villarrica mantle source was calculated from the Villarrica primitive average, and the trace element composition of the Villarrica mantle source was calculated from the best model fit in Fig. 8. Only a small percentage of mixing lines pass near Don Casimiro-Maipo. b-c) Trace element and isotopic signatures of the

mixed compositions that produce isotopic ratios close to Don Casimiro-Maipo (red lines in a), and have Eu/Eu*>0.9. None of these lithologies can recreate Sr, Ba and $^{87}Sr/^{86}Sr$ systematics at Don Casimiro-Maipo. Error bars show 1σ of primitive samples at Don Casimiro-Maipo and Villarrica based on 5 and 3 analyses respectively.

Fig. 10- Variation in rear-arc slab inputs. a) Mixing models of slab-sensitive ratios between a melt of a rear-arc mantle source (F=0.02, melting at 3.3 Gpa) that has not received slab inputs, and a melt of a rear-arc mantle source at the same conditions that has received slab inputs (20% sediment, 80% AOC). The orange wedge reflects progressive mixing of 10% slab (with ODP1232± 1σ) into a mantle source with 0% EM1 enrichment, and the green wedge reflects mixing of 17% slab (with ODP1232± 1σ) into a mantle source with 80% EM1 enrichment. Rear-arc trace element ratios follow these mixing lines remarkably closely, with the small amount of scatter likely explained by variable conditions of melting along the rear-arc. b) Trace element ratios sensitive to slab additions versus trench distance. MORB-like ratios (blue histogram; Gale et al., 2013) start to appear at distances greater than 425 km. Remarkably high, arc-like ratios (black histogram shows the range of these ratios at the SVZ arc-front) are seen up to 600 km from the trench, with large scatter in ratios at large trench distances, contrary to the narrow range of observed isotopes.

Fig. 11 –Isotopic compositions of inferred SCLM melts within South America (approximate locations on Fig. 2a). These clearly extend the array that passes from DMM/DAM through the arc-front and rear-arc, to Don Casimiro-Maipo. The field produced by contaminating the Villarrica mantle source with crustal lithologies (Fig. 9a) is also overlain (grey). This follows a much shallower trajectory than SCLM melts, and is significantly broader than the SCLM field. Mobile belt M-SCLM melts represent alkaline volcanics erupted on the edges of the Sao Fransisco craton and the Rio Apa-Luis Alves craton on the east coast of South America (Gibson et al., 1995; 2005 and Carlson et al., 1996). Southern Rift melts were erupted just north of the NSVZ (Lucassen et al., 2002). Carboniferous granitoids are from the Santo Domingo Complex of the Coastal Batholith (Parada et al., 1999). All are suggested to have sampled M-SCLM. The green and blue lines show a recycling model in which low degree melts are extracted from the depleted mantle (Salters and Stracke, 2004) and then aged for up to 2 Ga using the parameters from Stracke et al. (2003; see Turner et al., 2017). A model with F=0.003-0.008 encapsulates the range of isotopic compositions observed in SCLM melts.

Fig. 12- Schematic diagrams showing possible explanations for the isotopic enrichment minimum, and its relationship to tectonic features. a) A Permian suture zone corresponds with an absence of M-SCLM. b) A vertical and horizontal slab tear at ~39˚S may allow depleted Pacific MORB mantle to upwell, and dilute the EM1-type enrichment in the sub-arc mantle located above the tear. As the proportion of depleted Pacific MORB mantle declines northwards and southwards, isotopic signatures become more enriched. Upper plate geometry adapted from box model of Søager et al. (2015b), pp. 1514.

Fig. 13 –A unified model for the SVZ can account for the different trajectories of arc-front and rear-arc samples. a) Large variations in Ba/Th within arc-front and rear-arc olivines can be accounted for by variations in slab additions. For example, mafic enclaves from Longavi volcano show Ba/Th ratios up to ~500, which have been attributed to the subduction of the Mocho fracture zone beneath this centre (Rodriguez et al., 2007). b-d) Trace element and isotopic plots showing rear-arc and filtered SVZ arc-front samples (Eu/Eu*<0.9), along with the composition of the two mantle components used in this study (BAM, EM1), and the composition field of MORB (Gale et al., 2013). The composition of mafic enclaves from Longavi are shown to demonstrate the amount of variability that can be generated from the subducting slab. Melting

trajectories from the model described in section 4.2 are shown in c and d) to demonstrate the fractionation of certain trace element ratios by the low melt extents that likely dominate the rear-arc. The unit vector directions from BAM generated by varying different components are shown. Søager et al. (2013; 2015a) suggest that the offset trajectory of the SVZ arc-front and rear-arc in the cross plots shown in b-d are produced by LCC assimilation. However, the variability made available by varying degrees of EM1 enrichment, variable slab fluxes and variable melt extents can easily account for the offsets between these trajectories.

Fig. 14 – Schematic diagrams of rear-arc slab supply. a) Traditional model of slab supply, with buoyant rise of slab fluids to the rear-arc from a slab melting at higher pressure and temperature than at the arc-front. The composition of these fluids should change with increasing trench distance, as the depth to the slab increases. Additionally, at large trench distances, very little to no slab supply would be expected, due to the exhaustion of hydrous phases. b) Proposed model of this study, inspired by Cagniocle et al. (2007), Wilson et al. (2014) and Cerpa et al. (2017). Down dragging of fluids released at arc-front depths explains the similar composition of arc-front and rear-arc slab supply.

References

Annen, C., Blundy, J.D. and Sparks, R.S.J., 2006. The genesis of intermediate and silicic magmas in deep crustal hot zones. *Journal of Petrology*, **47(3)**, pp. 505-539.

Baasner, A., Médard, E., Laporte, D. and Hoffer, G., 2016. Partial melting of garnet lherzolite with water and carbon dioxide at 3 GPa using a new melt extraction technique: implications for intraplate magmatism. *Contributions to Mineralogy and Petrology*, **171(5)**, p.45.

Boyet, M., Doucelance, R., Israel, C., Bonnand, P., Auclair, D., Suchorski, K. and Bosq, C., New constraints on the origin of the EM-1 component revealed by the measurement of the La-Ce isotope systematics in Gough Island lavas. *Geochemistry, Geophysics, Geosystems*.

Brandt, F.E., Holm, P.M. and Søager, N., 2017. South-to-north pyroxenite–peridotite source variation correlated with an OIB-type to arc-type enrichment of magmas from the Payenia backarc of the Andean Southern Volcanic Zone (SVZ). *Contributions to Mineralogy and Petrology*, **172(1)**, pp. 1-25.

Burd, A.I., Booker, J.R., Mackie, R., Favetto, A. and Pomposiello, M.C., 2014. Three-dimensional electrical conductivity in the mantle beneath the Payun Matru volcanic field in the Andean backarc of Argentina near 36.5° S: evidence for decapitation of a mantle plume by resurgent upper mantle shear during slab steepening. *Geophysical Journal International*, **198**, pp. 812–827.

Cagnioncle, A.M., E. Parmentier, and L. T. Elkins-Tanton., 2007. Effect of solid flow above a subducting slab on water distribution and melting at convergent plate boundaries*.* *Journal of Geophysical Research*, **112 (B9).**

Cao, W., Lee, C.T.A. and Lackey, J.S., 2017. Episodic nature of continental arc activity since 750 Ma: A global compilation. *Earth and Planetary Science Letters*, **461, pp.85-95**.

Carlson, R.W., Esperanca, S. and Svisero, D.P., 1996. Chemical and Os isotopic study of Cretaceous potassic rocks from southern Brazil. *Contributions to Mineralogy and Petrology*, **125(4)**, pp.393-405.

Carter, L.B., Skora, S., Blundy, J.D., De Hoog, J.C.M. and Elliott, T., 2015. An experimental study of trace element fluxes from subducted oceanic crust. *Journal of Petrology*, **56(8)**, pp.1585-1606.

Cerpa, N.G., Wada, I. and Wilson, C., 2017. Fluid migration in the mantle wedge: Influence of mineral grain size and mantle compaction. *Journal of Geophysical Research: Solid Earth*, **122**, doi:10.1002/2017JB014046.

Chapman, J.B., Ducea, M.N., DeCelles, P.G. and Profeta, L., 2015. Tracking changes in crustal thickness during orogenic evolution with Sr/Y: An example from the North American Cordillera. *Geology*, **43(10)**, pp.919-922.

Charrier, R., 1979. Los Volcanes Andres y Don Casimiro: Dos centros descubiertos en los Andes entre 34° S Y 34° S 45' Latitud Sur. *Revista Geologica de Chile*, **8**, pp. 79–85.

Chiaradia, M., 2015. Crustal thickness control on Sr/Y signatures of recent arc magmas: an Earth scale perspective. *Scientific reports*, **5**, p.8115.

Cruz-Uribe, A.M., Marschall, H.R., Gaetani, G.A. and Le Roux, V., 2018. Generation of alkaline magmas in subduction zones by partial melting of mélange diapirs—An experimental study. *Geology*, **46(4)**, pp.343-346.

Davidson, J.P., McMillan, N.J., Moorbath, S., Wörner, G., Harmon, R.S. and Lopez-Escobar, L., 1990. The Nevados de Payachata volcanic region (18 S/69 W, N. Chile) II. Evidence for widespread crustal involvement in Andean magmatism. *Contributions to Mineralogy and Petrology*, **105(4)**, pp.412-432.

DePaolo, D.J., 1981. Trace element and isotopic effects of combined wallrock assimilation and fractional crystallization. *Earth and Planetary Science Letters*, **53(2)**, pp.189-202.

Dungan, M.A., Wulff, A. and Thompson, R., 2001. Eruptive stratigraphy of the Tatara–San Pedro complex, 36 S, Southern Volcanic Zone, Chilean Andes: reconstruction method and implications for magma evolution at long-lived arc volcanic centers. *Journal of Petrology*, **42(3)**, pp.555-626.

England, P., 2018. On shear stresses, temperatures, and the maximum magnitudes of earthquakes at convergent plate boundaries. *Journal of Geophysical Research*: Solid Earth.

Ewart, A. and Hawkesworth, C.J., 1987. The Pleistocene-Recent Tonga-Kermadec arc lavas: interpretation of new isotopic and rare earth data in terms of a depleted mantle source model. *Journal of Petrology*, **28(3)**, pp.495-530.

Farner, M.J. and Lee, C.T.A., 2017. Effects of crustal thickness on magmatic differentiation in subduction zone volcanism: A global study. *Earth and Planetary Science Letters*, **470**, pp.96-107.

Folguera, A., Naranjo, J.A., Orihashi, Y., Sumino, H., Nagao, K., Polanco, E. and Ramos, V.A., 2009. Retroarc volcanism in the northern San Rafael Block (34–35 30 S), southern Central Andes: Occurrence, age, and tectonic setting. *Journal of Volcanology and Geothermal Research*, **186(3)**, pp. 169-185.

Forni, F., Degruyter, W., Bachmann, O., De Astis, G. and Mollo, S., 2018. Long-term magmatic evolution reveals the beginning of a new caldera cycle at Campi Flegrei. *Science advances*, *4*(11), p.eaat9401.

Futa, K. and Stern, C.R., 1988. Sr and Nd isotopic and trace element compositions of Quaternary volcanic centers of the southern Andes. *Earth and Planetary Science Letters***, 88(3-4)**, pp.253-262.

Gale, A., Dalton, C. A., Langmuir, C. H., Su, Y. and Schilling, J. G., 2013. The Mean Composition of Ocean Ridge Basalts. *Geochemistry, Geophysics, Geosystems*, **14(3)**, pp. 489–518.

Gibson, S. A., Thompson, R. N., Day, J. A., Humphris, S. E. and Dickin, A. P., 2005. Melt-generation processes associated with the Tristan mantle plume: Constraints on the origin of EM-1. *Earth and Planetary Science Letters*, **237(3–4)**, pp. 744–767.

Gibson, S. A., Thompson, R. N., Leonardos, O. H., Dickin, A. P., Mitchell, J. G., Paranaiba, A. and Province, I., 1995. The Late Cretaceous Impact of the Trindade Mantle Plume : Evidence from Magmatism in SE Brazil. *Journal of Petrology***, 36 (1)**, pp. 189-229.

Gudnason, J., Holm, P.M., Søager, N. and Llambías, E.J., 2012. Geochronology of the late Pliocene to recent volcanic activity in the Payenia back-arc volcanic province, Mendoza Argentina. *Journal of South American Earth Sciences*, *37*, pp.191-201.

Hermann, J. and Rubatto, D., 2009. Accessory phase control on the trace element signature of sediment melts in subduction zones. *Chemical Geology*, **265(3–4)**, pp. 512–526.

Hermann, J. and Spandler, C.J., 2007. Sediment melts at sub-arc depths: an experimental study. *Journal of Petrology*, **49(4)**, pp.717-740.

Hickey, R.L., Frey, F.A., Gerlach, D.C. and Lopez-Escobar, L., 1986. Multiple sources for basaltic arc rocks from the southern volcanic zone of the Andes (34–41 S): trace element and isotopic evidence for contributions from subducted oceanic crust, mantle, and continental crust. *Journal of Geophysical Research: Solid Earth*, **91(B6)**, pp.5963-5983.

Hickey-Vargas, R., Holbik, S., Tormey, D., Frey, F.A. and Roa, H.M., 2016. Basaltic rocks from the Andean Southern Volcanic Zone: Insights from the comparison of along-strike and small-scale geochemical variations and their sources*.* *Lithos*, **258**, pp.115-132.

Hildreth, W. and Moorbath, S., 1988. Crustal contribution to arc magmatism in the Andes of Central Chile. *Contributions to Mineralogy and Petrology*, **98**, pp. 455–489.

Hildreth, W. and Moorbath, S., 1991. Reply to Comment on "Crustal contributions to arc magmatism in the Andes of Central Chile" by W. Hildreth and S. Moorbath*. Contributions to Mineralogy and Petrology***, 108(1)**, pp. 247-252.

Hirai, Y., Yoshida, T., Okamura, S., Tamura, Y., Sakamoto, I. and Shinjo, R., 2018. Breakdown of residual zircon in the Izu arc subducting slab during backarc rifting. *Geology*, **46(4)**, pp.371-374.

Hochstaedter, A., Gill, J., Peters, R., Broughton, P., Holden, P. and Taylor, B., 2001. Across-arc geochemical trends in the Izu-Bonin arc: Contributions from the subducting slab. *Geochemistry, Geophysics, Geosystems*, **2(7)**, 2000GC000105.

Holm, P.M., Søager, N., Alfastsen, M. and Bertotto, G.W., 2016. Subduction zone mantle enrichment by fluids and Zr–Hf-depleted crustal melts as indicated by backarc basalts of the Southern Volcanic Zone, Argentina. *Lithos*, **262**, pp. 135-152.

Holm, P.M., Søager, N., Dyhr, C.T. and Nielsen, M.R., 2014. Enrichments of the mantle sources beneath the Southern Volcanic Zone (Andes) by fluids and melts derived from abraded upper continental crust. *Contributions to Mineralogy and Petrology*, **167(5),** p.1004.

Jacques, G., Hoernle, K., Gill, J., Hauff, F., Wehrmann, H., Garbe-Schönberg, D., van den Bogaard, P., Bindeman, I. and Lara, L. E., 2013. Across-arc geochemical variations in the Southern Volcanic Zone, Chile (34.5-38.0° S): Constraints on mantle wedge and slab input compositions. *Geochimica et Cosmochimica Acta*, **123**, pp. 218–243.

Jacques, G., Hoernle, K., Gill, J., Wehrmann, H., Bindeman, I. and Lara, L. E., 2014. Geochemical variations in the Central Southern Volcanic Zone, Chile (38 – 43 ° S): The role of fluids in generating arc magmas. *Chemical Geology*, **371**, pp. 27–45.

Johnson, M. C., and Plank, T., 1999. Dehydration and melting experiments constrain the fate of subducted sediments*. Geochemistry, Geophysics, Geosystems***, 1(1)**, 1007, doi:10.1029/1999GC000014.

Karlstrom, L., Lee, C.T. and Manga, M., 2014. The role of magmatically driven lithospheric thickening on arc front migration. *Geochemistry, Geophysics, Geosystems***, 15(6)**, pp.2655-2675.

Kay, S.M., Orrell, S. and Abbruzzi, J.M., 1996. Zircon and whole rock Nd-Pb isotopic evidence for a Grenville age and a Laurentian origin for the basement of the Precordillera in Argentina. *The Journal of Geology*, *104*(6), pp.637-648.

Kay, S.M. and Copeland, P., 2006. Early to middle Miocene backarc magmas of the Neuquén Basin: Geochemical consequences of slab shallowing and the westward drift of South America. *Geological Society of America Special Papers***, 407(9)**, pp. 185–213.

Kay, S.M., Godoy, E. and Kurtz, A., 2005. Episodic arc migration, crustal thickening, subduction erosion, and magmatism in the south-central Andes. *Bulletin of the Geological Society of America*, **117(1–2)**, pp. 67–88.

Kay, S.M., Jones, H.A. and Kay, R.W., 2013. Origin of Tertiary to Recent EM1 and subduction-like chemical and isotopic signatures in Auca Mahuida region (37-38S) and other Patagonian plateau lavas. *Contributions to Mineralogy and Petrology*, **166(1)**, pp. 165–192.

Kessel, R., Schmidt, M.W., Ulmer, P. and Pettke, T., 2005. Trace element signature of subduction-zone fluids, melts and supercritical liquids at 120–180 km depth. *Nature*, **437(7059)**, p.724.

Klaver, M., Davies, G.R. and Vroon, P.Z., 2016. Subslab mantle of African provenance infiltrating the Aegean mantle wedge. *Geology*, **44(5)**, pp. 367-370.

Knott, T.R., Branney, M.J., Reichow, M.K., Finn, D.R., Coe, R.S., Storey, M., Barfod, D. and McCurry, M., 2016. Mid-Miocene record of large-scale Snake River–type explosive volcanism and associated subsidence on the Yellowstone hotspot track: The Cassia Formation of Idaho, USA. *Bulletin*, *128*(7-8), pp.1121-1146.

Leeman, W.P., 1983. The influence of crustal structure on compositions of subduction-related magmas. *Journal of Volcanology and Geothermal Research*, **18(1-4),** pp.561-588.

Lopez-Escobar, L., Frey, F.A. and Vergara, M., 1977. Andesites and high-alumina basalts from the central-south Chile High Andes: geochemical evidence bearing on their petrogenesis. *Contributions to Mineralogy and Petrology*, **63(3)**, pp.199-228.

Lucassen, F., Becchio, R., Harmon, R., Kasemann, S., Franz, G., Trumbull, R., Wilke, H., Romer, R. L. and Dulski, P., 2001. Composition and density model of the continental crust at an active continental margin — the Central Andes between 21 ° S and 27 ° S. *Tectonophysics,* **341(1)**, pp. 195–223.

Lucassen, F., Escayola, Æ. M., Romer, A. R. L., Kerstin, V. Æ. and Gerhard, K. Æ., 2002. Isotopic composition of Late Mesozoic basic and ultrabasic rocks from the Andes (23 – 32 ° S) – implications for the Andean mantle. *Contributions to Mineralogy and Petrology*, **143(3)** pp. 336–349.

Lucassen, F., Kramer, W., Bartsch, V., Wilke, H.G., Franz, G., Romer, R.L. and Dulski, P., 2006. Nd, Pb, and Sr isotope composition of juvenile magmatism in the Mesozoic large magmatic province of northern Chile (18–27 S): indications for a uniform subarc mantle. *Contributions to Mineralogy and Petrology***, 152(5)**, p.571.

Lucassen, F., Trumbull, R., Franz, G., Creixell, C., Vásquez, P., Romer, R. L. and Figueroa, O., 2004. Distinguishing crustal recycling and juvenile additions at active continental margins: The Paleozoic to recent compositional evolution of the Chilean Pacific margin (36-41° S). *Journal of South American Earth Sciences*, **17(2)**, pp. 103–119.

MacDougall, J.G., Jadamec, M.A. and Fischer, K.M., 2017. The zone of influence of the subducting slab in the asthenospheric mantle. *Journal of Geophysical Research: Solid Earth*, *122*(8), pp.6599-6624.

McDonough, W.F. and Sun, S.S., 1995. The composition of the Earth. *Chemical Geology*, **120**, pp. 223-253.

McKenzie, D.A.N. and O'Nions, R.K., 1995. The source regions of ocean island basalts. *Journal of Petrology*, **36(1)**, pp.133-159.

Orozco, G., Garces, F., Jara, G., and Lara, L.E., 2015. Nuevos antecedentes para la geología del complejo volcánico Maipo-Diamante, Andes del Sur. Congreso Geologico Chileno, La Serena, Octubre 2015. (abstract – accessed http://biblioteca.sernageomin.cl/opac/DataFiles/14905_v3_pp_218_221.pdf, 13th January, 2018).

Pallares, C., Quidelleur, X., Gillot, P.Y., Kluska, J.M., Tchilinguirian, P. and Sarda, P., 2016. The temporal evolution of back-arc magmas from the Auca Mahuida shield volcano (Payenia Volcanic Province, Argentina). *Journal of Volcanology and Geothermal Research*, *323*, pp.19-37.

Parada, M.A., Nyström, J.O. and Levi, B.., 1999. Multiple sources for the Coastal Batholith of central Chile (31–34 S): geochemical and Sr–Nd isotopic evidence and tectonic implications. *Lithos*, **46(3)**, pp.505-521.

Pearce, J.A., Kempton, P.D. and Gill, J.B., 2007. Hf–Nd evidence for the origin and distribution of mantle domains in the SW Pacific*. Earth and Planetary Science Letters*, **260(1)**, pp.98-114.

Penniston-Dorland, S.C., Kohn, M.J. and Manning, C.E., 2015. The global range of subduction zone thermal structures from exhumed blueschists and eclogites: Rocks are hotter than models. *Earth and Planetary Science Letters*, **428**, pp.243-254.

Pesicek, J. D., Engdahl, E. R., Thurber, C. H., Deshon, H. R. and Lange, D., 2012. Mantle subducting slab structure in the region of the 2010 M8.8 Maule earthquake (30-40° S), Chile. *Geophysical Journal International*, **191(1)**, pp. 317–324.

Plank, T. and Langmuir, C.H., 1988. An evaluation of the global variations in the major element chemistry of arc basalts. *Earth and Planetary Science Letters*, **90**, pp. 349–370.

Plank, T., 2005. Constraints from thorium/lanthanum on sediment recycling at subduction zones and the evolution of the continents. *Journal of Petrology*, **46(5)**, pp.921-944.

Profeta, L., Ducea, M.N., Chapman, J.B., Paterson, S.R., Gonzales, S.M.H., Kirsch, M., Petrescu, L. and DeCelles, P.G., 2015. Quantifying crustal thickness over time in magmatic arcs. *Scientific Reports*, **5**, p.17786.

Ramos, V.A., 2010. The Grenville-age basement of the Andes, *Journal of South American Earth Sciences*, **29**, pp. 77–91.

Ramos, V.A. and Folguera, A., 2011. Payenia volcanic province in the Southern Andes: An appraisal of an exceptional Quaternary tectonic setting. *Journal of Volcanology and Geothermal Research*, **201(1–4)**, pp. 53–64.

Rapalini, A.E., de Luchi, M.G.L., Dopico, C.M., Klinger, F.G.L., Giménez, M.E., Martínez, P., 2010. Did Patagonia collide with Gondwana in the Late Paleozoic? Some insights from a multidisciplinary study of magmatic units of the North Patagonian Massif. *Geologica Acta*, **8**, 349-371.

RodrÍguez, C., Sellés, D., Dungan, M., Langmuir, C. and Leeman, W., 2007. Adakitic dacites formed by intracrustal crystal fractionation of water-rich parent magmas at Nevado de Longaví volcano (36· 2 S; Andean Southern Volcanic Zone, Central Chile). *Journal of Petrology*, *48*(11), pp.2033-2061.

Rogers, G. and Hawkesworth, C.J., 1989. A geochemical traverse across the North Chilean Andes: evidence for crust generation from the mantle wedge. *Earth and Planetary Science Letters*, **91**, pp. 271-285.

Rudnick, R.L. and Gao, S., 2003. Composition of the continental crust. In: *Treatise on Geochemistry: The Crust* (Eds. R. Rudnick), **vol. 3**. Permagon, New York, pp. 1–64.

Ruscitto, D.M., Wallace, P.J., Cooper, L.B. and Plank, T., 2012. Global variations in H2O/Ce: 2. Relationships to arc magma geochemistry and volatile fluxes. *Geochemistry, Geophysics, Geosystems*, **13(3).**

Salters, V.J. and Stracke, A., 2004. Composition of the depleted mantle. *Geochemistry, Geophysics, Geosystems*, **5(5)**.

Savov, I.P., Ryan, J.G., D'Antonio, M. and Fryer, P., 2007. Shallow slab fluid release across and along the Mariana arc-basin system: Insights from geochemistry of serpentinized peridotites from the Mariana fore arc. *Journal of Geophysical Research: Solid Earth*, **112(B9).**

Schmidt, M.W. and Jagoutz, O., 2017. The global systematics of primitive arc melts. *Geochemistry, Geophysics, Geosystems*, **18(8)**, pp.2817-2854.

Scott, E.M., Allen, M.B., Macpherson, C.G., McCaffrey, K.J., Davidson, J.P., Saville, C. and Ducea, M.N., 2018. Andean surface uplift constrained by radiogenic isotopes of arc lavas. *Nature Communications*, **9(1)**, p.969.

Sisson, T.W. and Kelemen, P.B., 2018. Near-solidus melts of MORB+ 4 wt% H 2 O at 0.8–2.8 GPa applied to issues of subduction magmatism and continent formation. *Contributions to Mineralogy and Petrology*, **173(9)**, p.70.

Skora, S. and Blundy, J., 2010. High-pressure hydrous phase relations of radiolarian clay and implications for the involvement of subducted sediment in arc magmatism. *Journal of Petrology*, **51(11)**, pp.2211-2243.

Søager, N. and Holm, P.M., 2013. Melt-peridotite reactions in upwelling eclogite bodies: Constraints from EM1-type alkaline basalts in Payenia, Argentina. *Chemical Geology*, **360–361**, pp. 204–219.

Søager, N., Holm, P.M. and Llambías, E.J., 2013. Payenia volcanic province, southern mendoza, argentina: OIB mantle upwelling in a backarc environment. *Chemical Geology*, **349–350**, pp. 36–53.

Søager, N., Martin, P. and Thirlwall, M.F., 2015a. Sr , Nd , Pb and Hf isotopic constraints on mantle sources and crustal contaminants in the Payenia volcanic province, Argentina. *Lithos*, **212–215**, pp. 368–378.

Søager, N., Portnyagin, M., Hoernle, K., Holm, P. M., Hauff, F. and Garbe-Schanberg, D., 2015b. Olivine major and trace element compositions in Southern Payenia Basalts, Argentina: Evidence for pyroxenite-peridotite melt mixing in a back-arc setting. *Journal of Petrology*, **56(8)**, pp. 1495–1518.

Sobolev, A. V., Hofmann, A. W., Kuzmin, D. V., Yaxley, G. M., Arndt, N. A., Chung, S.-L., Danyushevsky, L. V., Elliott, T., Frey, F. A., Garcia, M. O., Gurenko, A. A., Kamenetsky, V. S., Kerr, A. C., Krivolutskaya, N. A., Matvienkov, V. V., Nikogosian, I. K., Rocholl, A., Sigurdsson, I. A., Sushchevskaya, N. M. and Teklay, M., 2007. The amount of recycled crust in sources of mantle derived melts. *Science,* **316**, pp. 412–417.

Spandler, C., Mavrogenes, J. and Hermann, J., 2007. Experimental constraints on element mobility from subducted sediments using high-P synthetic fluid/melt inclusions*. Chemical Geology*, **239(3)**, pp.228-249.

Sruoga, P., Llambías, E.J., Fauqué, L., Schonwandt, D. and Repol, D.G., 2005. Volcanological and geochemical evolution of the Diamante Caldera–Maipo volcano complex in the southern Andes of Argentina (34 10 S). *Journal of South American Earth Sciences*, **19(4)**, pp.399-414.

Stern, C.R., 1989. Pliocene to present migration of the volcanic front, Andean Southern Volcanic Zone. *Andean Geology*, **16(2)**, pp.145-162.

Stern, C.R., 2011. Subduction erosion: rates, mechanisms, and its role in arc magmatism and the evolution of the continental crust and mantle. *Gondwana Research*, *20*(2-3), pp.284-308.

Stracke, A., Bizimis, M. and Salters, V.J., 2003. Recycling oceanic crust: Quantitative constraints. *Geochemistry, Geophysics, Geosystems*, **4(3).**

Syracuse, E. M., van Keken, P. E., Abers, G. A., Suetsugu, D., Bina, C., Inoue, T., Wiens, D. and Jellinek, M., 2010. The global range of subduction zone thermal models, *Physics of the Earth and Planetary Interiors*, **183(1–2)**, pp. 73–90.

Tassara, A. and Echaurren, A., 2012. Anatomy of the Andean subduction zone: Three-dimensional density model upgraded and compared against global-scale models. *Geophysical Journal International*, **189(1)**, pp. 161–168.

Tormey, D., Hickey-Vargas, R., Frey, F., Lopez-Escobar, L., 1991. Recent lavas from the Andean front (32 to 42° S); Interpretations of along-arc compositional variations. *Geological Society of America, Special Paper*, **265**, pp. 57–77.

Turner, S.J. and Langmuir, C.H., 2015a. The global chemical systematics of arc front stratovolcanoes: Evaluating the role of crustal processes. *Earth and Planetary Science Letters*, **422**, pp.182-193.

Turner, S. J., and Langmuir, C. H., 2015b, What processes control the chemical compositions of arc front stratovolcanoes? *Geochemistry, Geophysics, Geosystems*, **16**, pp. 1865–1893.

Turner, S. J., Langmuir, C. H., Katz, R. F., Dungan, M. A. and Escrig, S., 2016. Parental arc magma compositions dominantly controlled by mantle-wedge thermal structure. *Nature Geoscience*, **9**, pp. 772-776,

Turner, S.J., Langmuir, C.H., Dungan, M.A. and Escrig, S., 2017. The importance of mantle wedge heterogeneity to subduction zone magmatism and the origin of EM1. *Earth and Planetary Science Letter*s, **472**, pp.216-228.

Valdenegro, P., Muñoz, M., Yáñez, G., Parada, M.A. and Morata, D., 2019. A model for thermal gradient and heat flow in central Chile: The role of thermal properties. *Journal of South American Earth Sciences*, *91*, pp.88-101.

Völker, D., Kutterolf, S. and Wehrmann, H., 2011. Comparative mass balance of volcanic edifices at the southern volcanic zone of the Andes between 33 S and 46 S. *Journal of Volcanology and Geothermal Research*, **205(3-4)**, pp.114-129.

Völker, D., Geersen, J., Contreras-Reyes, E. and Reichert, C., 2013. Sedimentary fill of the Chile Trench (32–46° S): volumetric distribution and causal factors. *Journal of the Geological Society*, *170*(5), pp.723-736.

Wang, J., Li, L., Xiong, X., 2016. Trace Element Partitioning during Hydrous Mantle Melting and Source Mineralogy of Arc Basalts. *Goldschmidt Conference Abstracts*, **3322**.

Willbold, M. and Stracke, A. 2010. Formation of enriched mantle components by recycling of upper and lower continental crust. *Chemical Geology*, **276(3–4)**, pp. 188–197.

Wilson, C.R., Spiegelman, M., van Keken, P.E. and Hacker, B.R., 2014. Fluid flow in subduction zones: the role of solid rheology and compaction pressure. *Earth and Planetary Science Letters*, **401**, pp. 261–274.

Woodhead, J., Stern, R.J., Pearce, J., Hergt, J., Vervoort, J., 2012. Hf-Nd isotope variation in Mariana Trough basalts: The importance of “ambient mantle” in the interpretation of subduction zone magmas. *Geology*, **40**, pp. 539-542

Workman, R.K. and Hart, S.R., 2005. Major and trace element composition of the depleted MORB mantle (DMM). *Earth and Planetary Science Letters*, **231(1–2)**, pp. 53–72.

Zandt, G. and Humphreys, E., 2008. Toroidal mantle flow around the western US slab window. *Geology*, **36(4)**, pp. 295-298.

Zindler A., and Hart S., 1986. Chemical Geodynamics. *Annual Review of Earth Planetary Sciences*, **14**, pp. 493–571

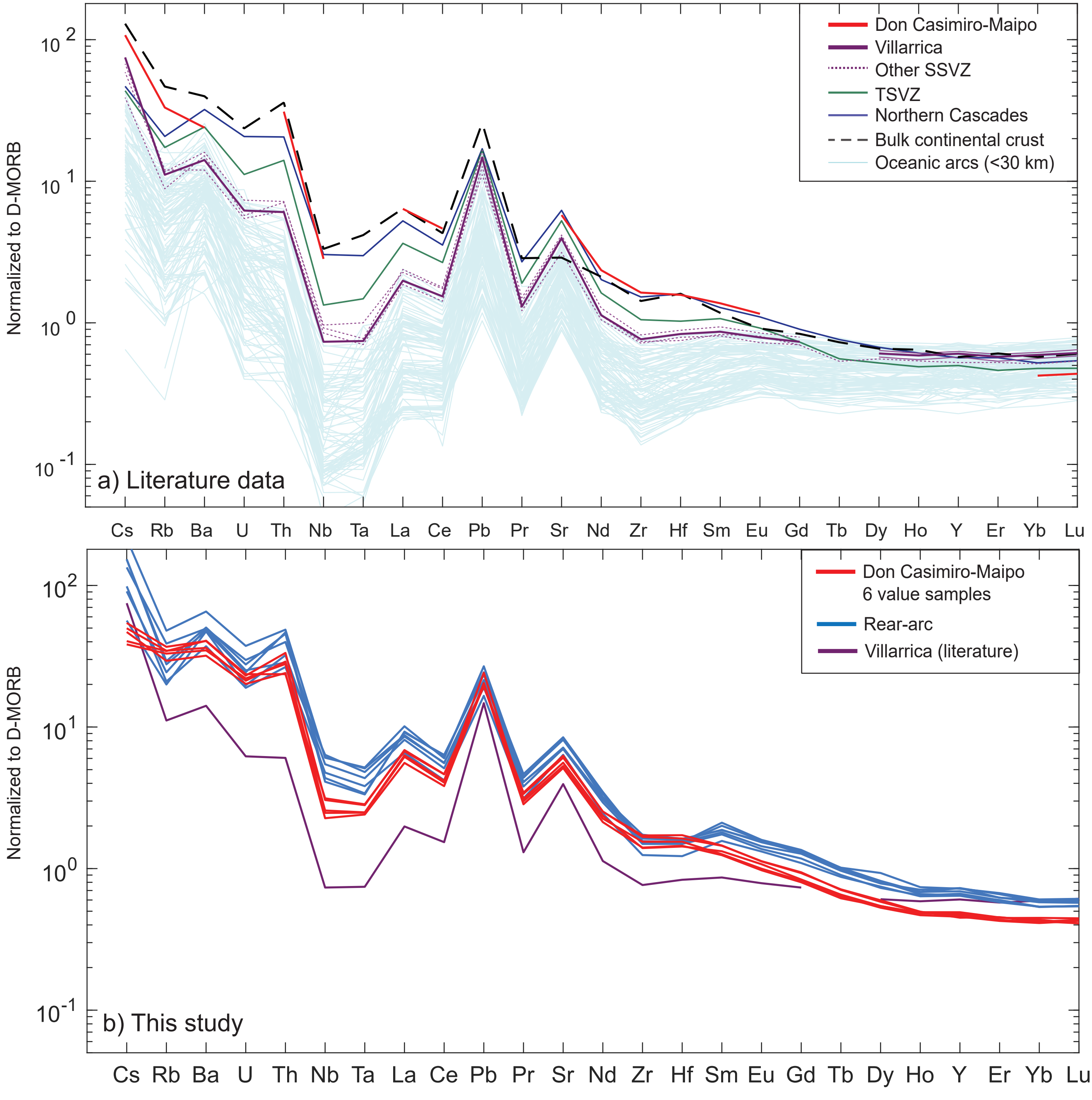
a) Literature data
Normalized to D-MORB
10 2
10 1
10 0
10 -1
Don Casimiro-Maipo
Villarrica
Other SSVZ
TSVZ
Northern Cascades
Bulk continental crust
Oceanic arcs (<30 km)
Cs Rb Ba U Th Nb Ta La Ce Pb Pr Sr Nd Zr Hf Sm Eu Gd Tb Dy Ho Y Er Yb Lu
b) This study
Normalized to D-MORB
10 2
10 1
10 0
10 -1
Don Casimiro-Maipo
6 value samples
Rear-arc
Villarrica (literature)
Cs Rb Ba U Th Nb Ta La Ce Pb Pr Sr Nd Zr Hf Sm Eu Gd Tb Dy Ho Y Er Yb Lu

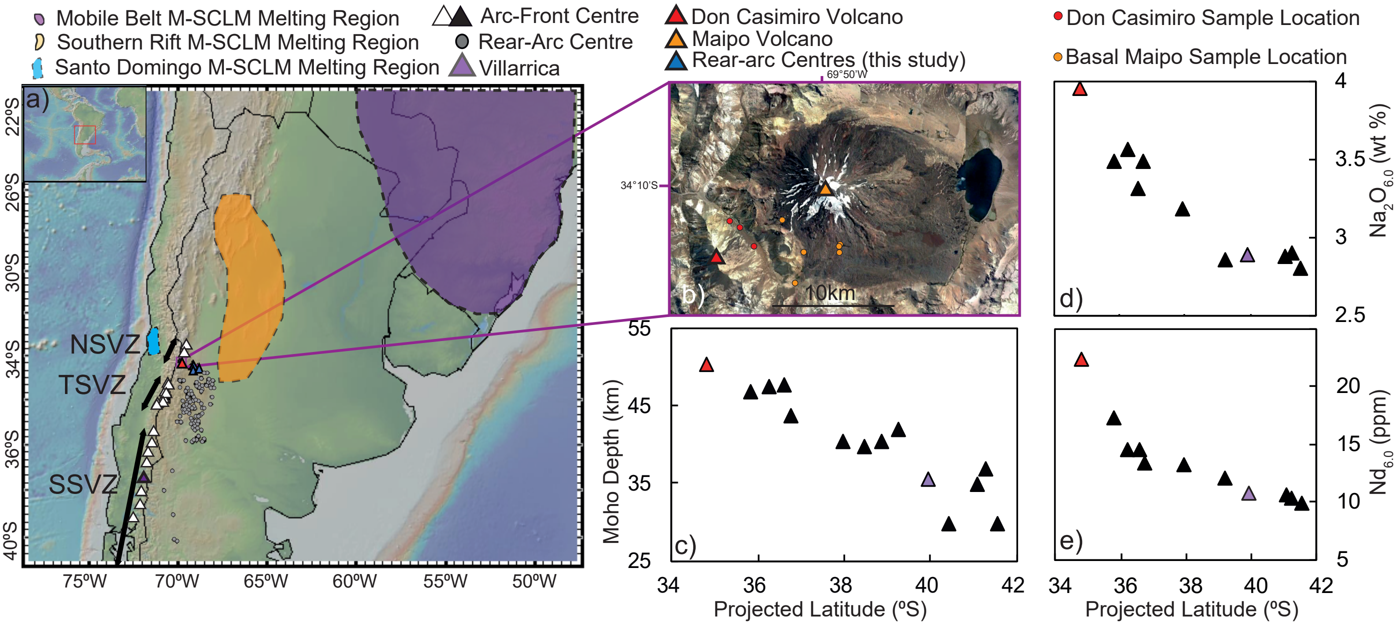
Mobile Belt M-SCLM Melting Region
Southern Rift M-SCLM Melting Region
Santo Domingo M-SCLM Melting Region
Arc-Front Centre
Rear-Arc Centre
Villarrica
Don Casimiro Volcano
Maipo Volcano
Rear-arc Centres (this study)
Don Casimiro Sample Location
Basal Maipo Sample Location
a)
22°S
26°S
30°S
34°S
36°S
40°S
NSVZ
TSVZ
SSVZ
75°W
70°W
65°W
60°W
55°W
50°W
69°50'W
34°10'S
b)
10km
c)
Moho Depth (km)
55
45
35
25
34
36
38
40
42
Projected Latitude (°S)
d)
$Na_2O_{6.0}$ (wt %)
4
3.5
3
2.5
e)
$Nd_{6.0}$ (ppm)
20
15
10
5
34
36
38
40
42
Projected Latitude (°S)

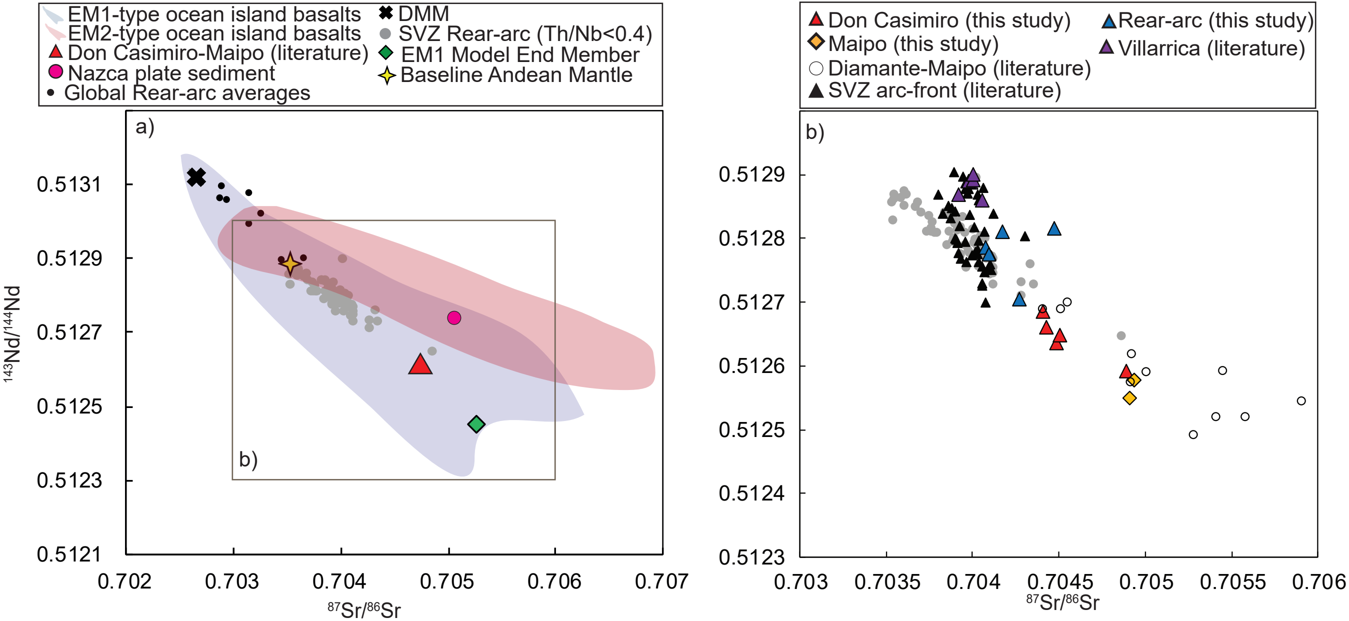
EM1-type ocean island basalts
EM2-type ocean island basalts
Don Casimiro-Maipo (literature)
Nazca plate sediment
Global Rear-arc averages
DMM
SVZ Rear-arc (Th/Nb<0.4)
EM1 Model End Member
Baseline Andean Mantle
a)
b)
0.5131
0.5129
0.5127
0.5125
0.5123
0.5121
$^{143}Nd/^{144}Nd$
0.702
0.703
0.704
0.705
0.706
0.707
$^{87}Sr/^{86}Sr$
Don Casimiro (this study)
Maipo (this study)
Diamante-Maipo (literature)
SVZ arc-front (literature)
Rear-arc (this study)
Villarrica (literature)
b)
0.5129
0.5128
0.5127
0.5126
0.5125
0.5124
0.5123
0.703
0.7035
0.704
0.7045
0.705
0.7055
0.706
$^{87}Sr/^{86}Sr$

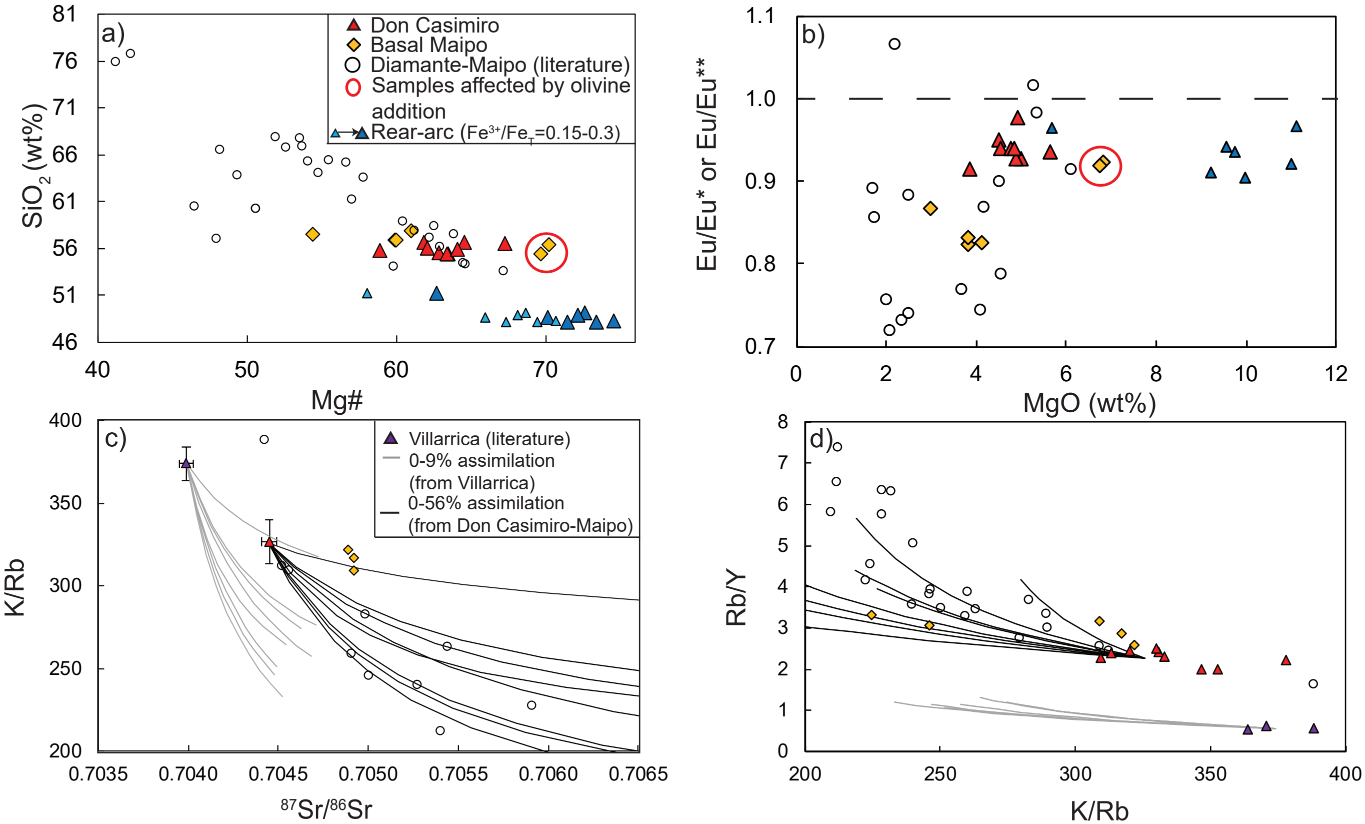
a)
Don Casimiro
Basal Maipo
Diamante-Maipo (literature)
Samples affected by olivine addition
Rear-arc (Fe^{3+}/Fe_T=0.15-0.3)
SiO_2 (wt%)
81
76
71
66
61
56
51
46
Mg#
40
50
60
70
b)
Eu/Eu* or Eu/Eu**
1.1
1.0
0.9
0.8
0.7
MgO (wt%)
0
2
4
6
8
10
12
c)
Villarrica (literature)
0-9% assimilation (from Villarrica)
0-56% assimilation (from Don Casimiro-Maipo)
K/Rb
400
350
300
250
200
$^{87}Sr/^{86}Sr$
0.7035
0.7040
0.7045
0.7050
0.7055
0.7060
0.7065
d)
Rb/Y
8
7
6
5
4
3
2
1
0
K/Rb
200
250
300
350
400

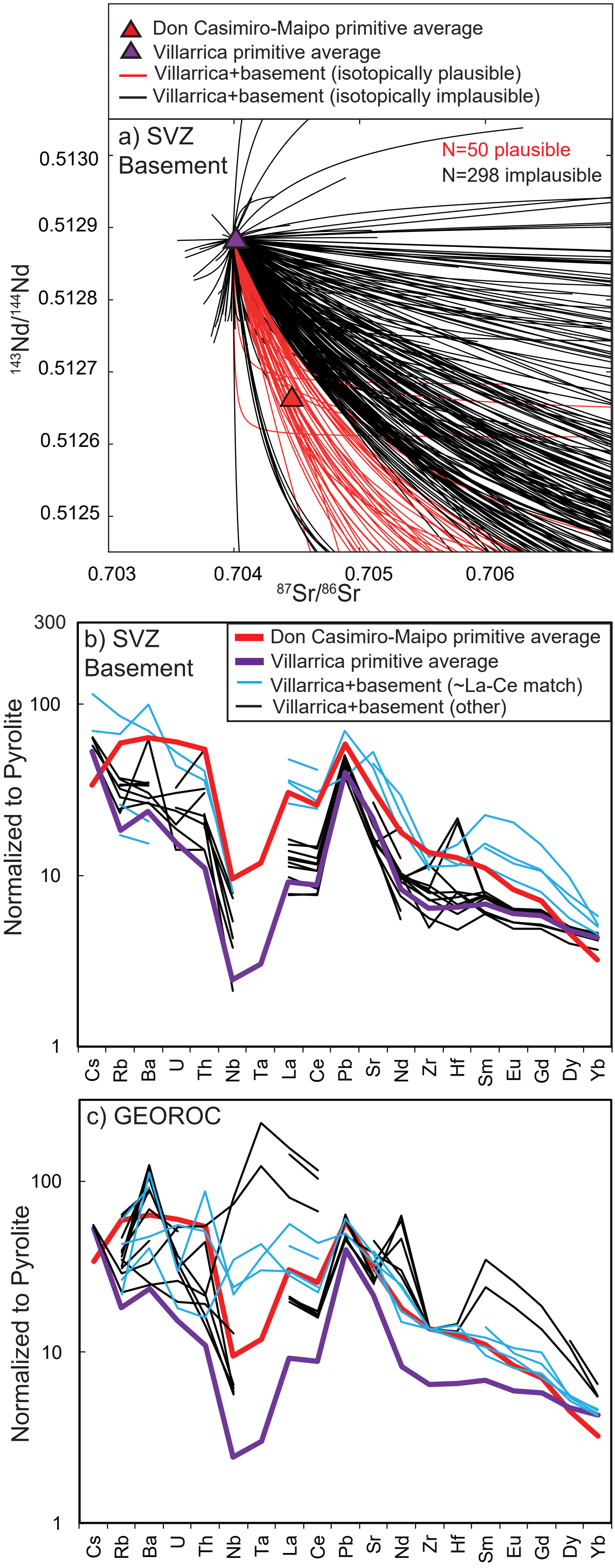
Don Casimiro-Maipo primitive average
Villarrica primitive average
Villarrica+basement (isotopically plausible)
Villarrica+basement (isotopically implausible)
a) SVZ
Basement
N=50 plausible
N=298 implausible
$^{143}Nd/^{144}Nd$
0.5130
0.5129
0.5128
0.5127
0.5126
0.5125
0.703
0.704
0.705
0.706
$^{87}Sr/^{86}Sr$
b) SVZ
Basement
Don Casimiro-Maipo primitive average
Villarrica primitive average
Villarrica+basement (~La-Ce match)
Villarrica+basement (other)
Normalized to Pyrolite
300
100
10
1
Cs
Rb
Ba
U
Th
Nb
Ta
La
Ce
Pb
Sr
Nd
Zr
Hf
Sm
Eu
Gd
Dy
Yb
c) GEOROC
Normalized to Pyrolite
100
10
1
Cs
Rb
Ba
U
Th
Nb
Ta
La
Ce
Pb
Sr
Nd
Zr
Hf
Sm
Eu
Gd
Dy
Yb

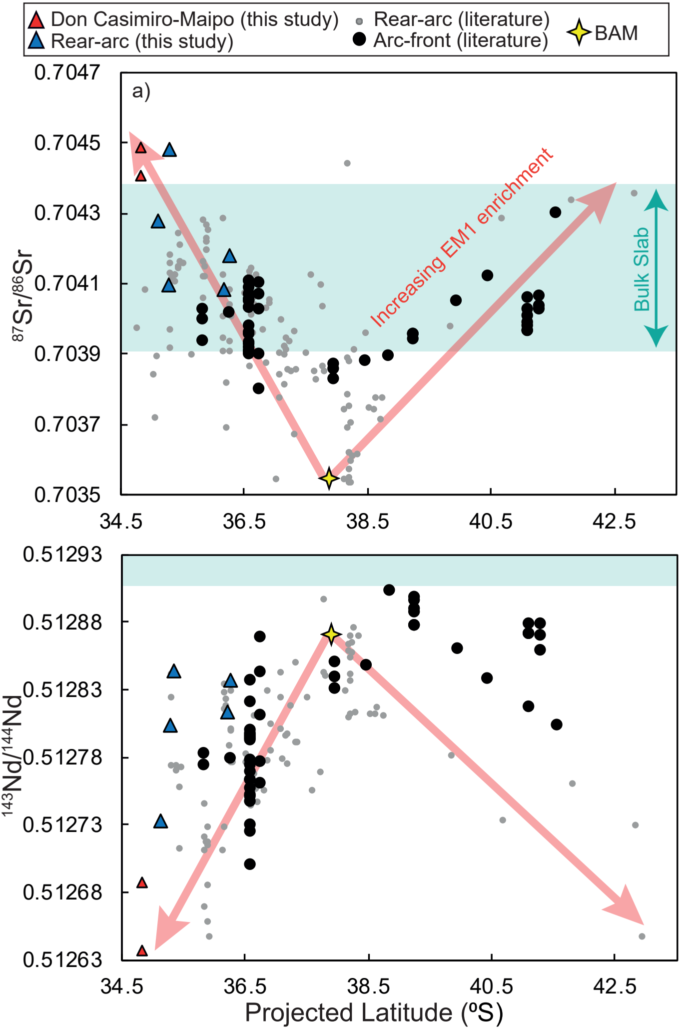
Don Casimiro-Maipo (this study)
Rear-arc (this study)
Rear-arc (literature)
Arc-front (literature)
BAM
a)
Increasing EM1 enrichment
Bulk Slab
^{87}Sr/^{86}Sr
0.7047
0.7045
0.7043
0.7041
0.7039
0.7037
0.7035
34.5
36.5
38.5
40.5
42.5
^{143}Nd/^{144}Nd
0.51293
0.51288
0.51283
0.51278
0.51273
0.51268
0.51263
Projected Latitude (ºS)

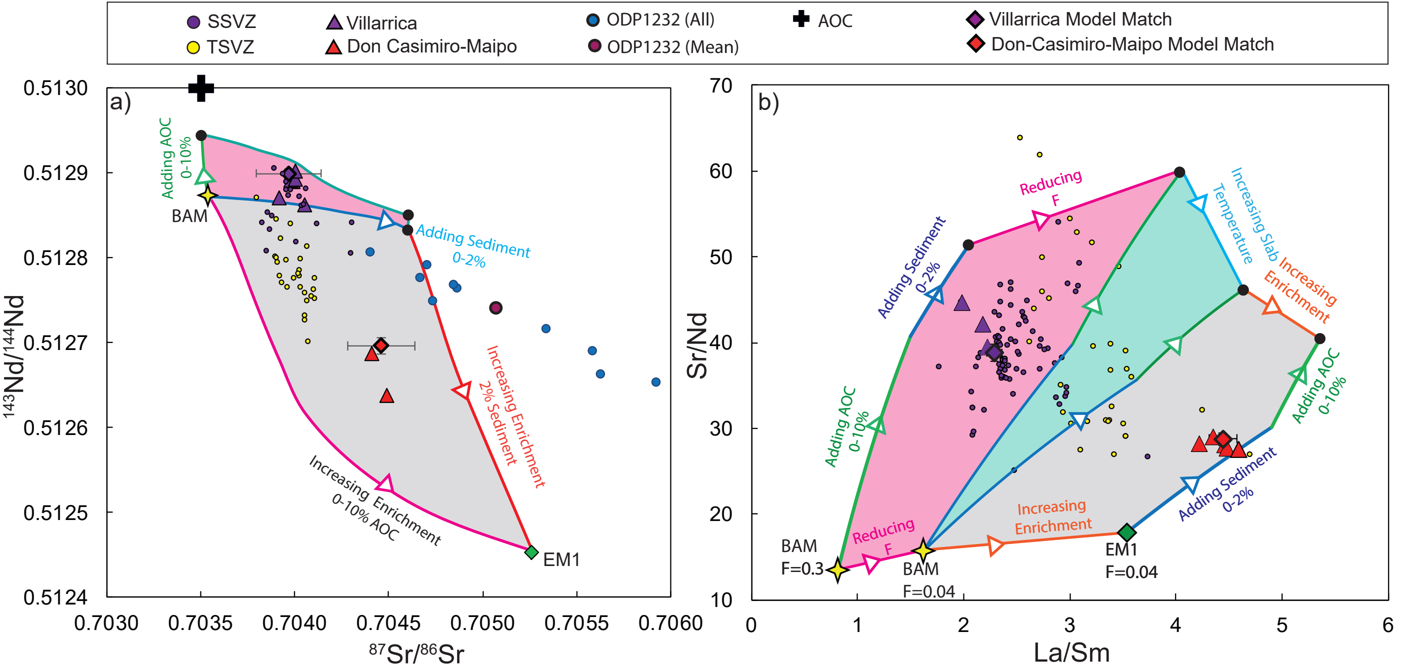
SSVZ
TSVZ
Villarrica
Don Casimiro-Maipo
ODP1232 (All)
ODP1232 (Mean)
AOC
Villarrica Model Match
Don-Casimiro-Maipo Model Match
a)
0.5130
0.5129
0.5128
0.5127
0.5126
0.5125
0.5124
$^{143}Nd/^{144}Nd$
0.7030
0.7035
0.7040
0.7045
0.7050
0.7055
0.7060
$^{87}Sr/^{86}Sr$
Adding AOC
0-10%
BAM
Adding Sediment
0-2%
Increasing Enrichment
2% Sediment
Increasing Enrichment
0-10% AOC
EM1
b)
70
60
50
40
30
20
10
Sr/Nd
0
1
2
3
4
5
6
La/Sm
Reducing
F
Adding Sediment
0-2%
Increasing
Temperature
Increasing Slab
Increasing
Enrichment
Adding AOC
0-10%
Adding AOC
0-10%
Adding Sediment
0-2%
Increasing
Enrichment
Reducing
F
BAM
F=0.3
BAM
F=0.04
EM1
F=0.04

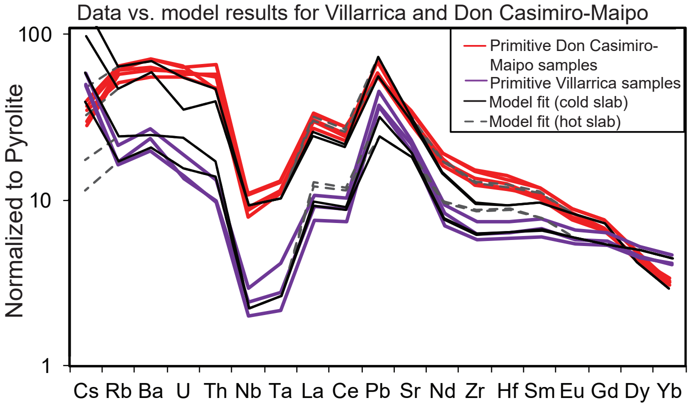
Data vs. model results for Villarrica and Don Casimiro-Maipo
Primitive Don Casimiro-Maipo samples
Primitive Villarrica samples
Model fit (cold slab)
Model fit (hot slab)
Normalized to Pyrolite
100
10
1
Cs
Rb
Ba
U
Th
Nb
Ta
La
Ce
Pb
Sr
Nd
Zr
Hf
Sm
Eu
Gd
Dy
Yb

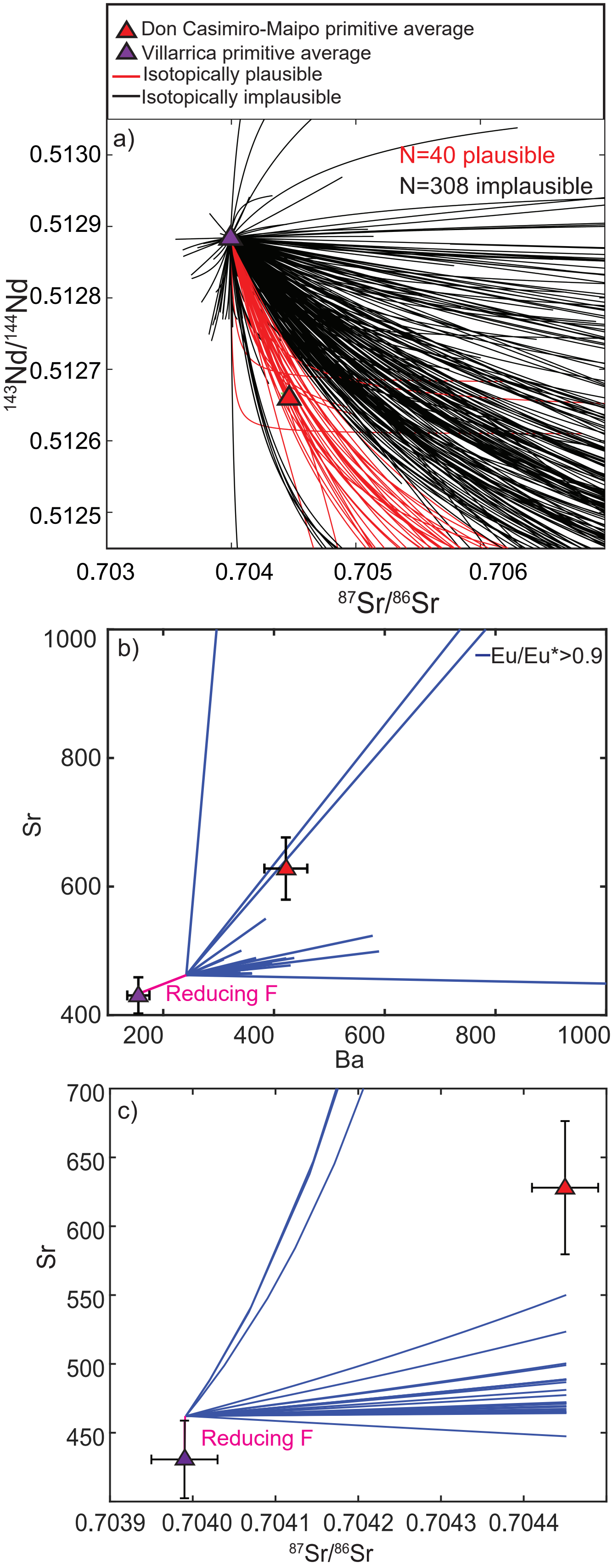
Don Casimiro-Maipo primitive average
Villarrica primitive average
Isotopically plausible
Isotopically implausible
a)
N=40 plausible
N=308 implausible
$^{143}Nd/^{144}Nd$
0.5130
0.5129
0.5128
0.5127
0.5126
0.5125
0.703
0.704
0.705
0.706
$^{87}Sr/^{86}Sr$
b)
Eu/Eu*>0.9
Reducing F
Sr
1000
800
600
400
200
400
600
800
1000
Ba
c)
Reducing F
Sr
700
650
600
550
500
450
0.7039
0.7040
0.7041
0.7042
0.7043
0.7044
$^{87}Sr/^{86}Sr$

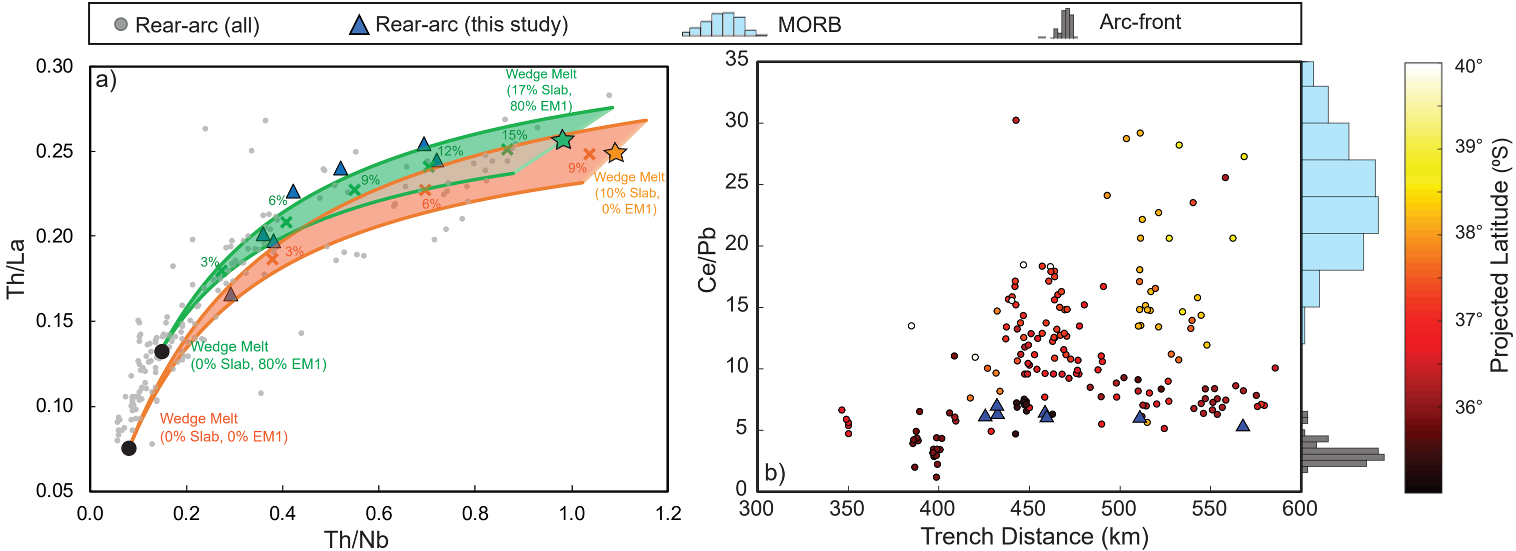
Rear-arc (all)
Rear-arc (this study)
MORB
Arc-front
a)
Th/La
Th/Nb
0.30
0.25
0.20
0.15
0.10
0.05
0.0
0.2
0.4
0.6
0.8
1.0
1.2
Wedge Melt (17% Slab, 80% EM1)
Wedge Melt (10% Slab, 0% EM1)
Wedge Melt (0% Slab, 80% EM1)
Wedge Melt (0% Slab, 0% EM1)
3%
6%
9%
12%
15%
3%
6%
9%
b)
Ce/Pb
Trench Distance (km)
0
5
10
15
20
25
30
35
300
350
400
450
500
550
600
Projected Latitude (°S)
40°
39°
38°
37°
36°

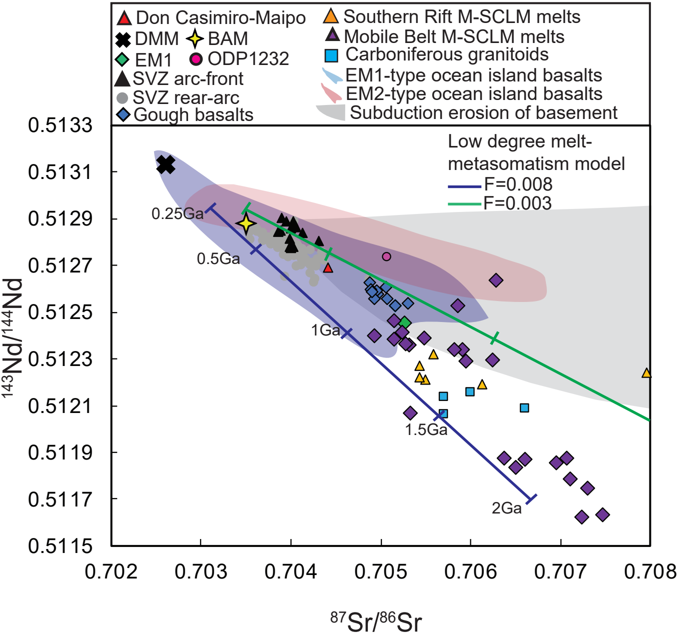
Don Casimiro-Maipo
DMM
BAM
EM1
ODP1232
SVZ arc-front
SVZ rear-arc
Gough basalts
Southern Rift M-SCLM melts
Mobile Belt M-SCLM melts
Carboniferous granitoids
EM1-type ocean island basalts
EM2-type ocean island basalts
Subduction erosion of basement
Low degree melt-metasomatism model
F=0.008
F=0.003
0.25Ga
0.5Ga
1Ga
1.5Ga
2Ga
0.5133
0.5131
0.5129
0.5127
0.5125
0.5123
0.5121
0.5119
0.5117
0.5115
^{143}Nd/^{144}Nd
0.702
0.703
0.704
0.705
0.706
0.707
0.708
^{87}Sr/^{86}Sr

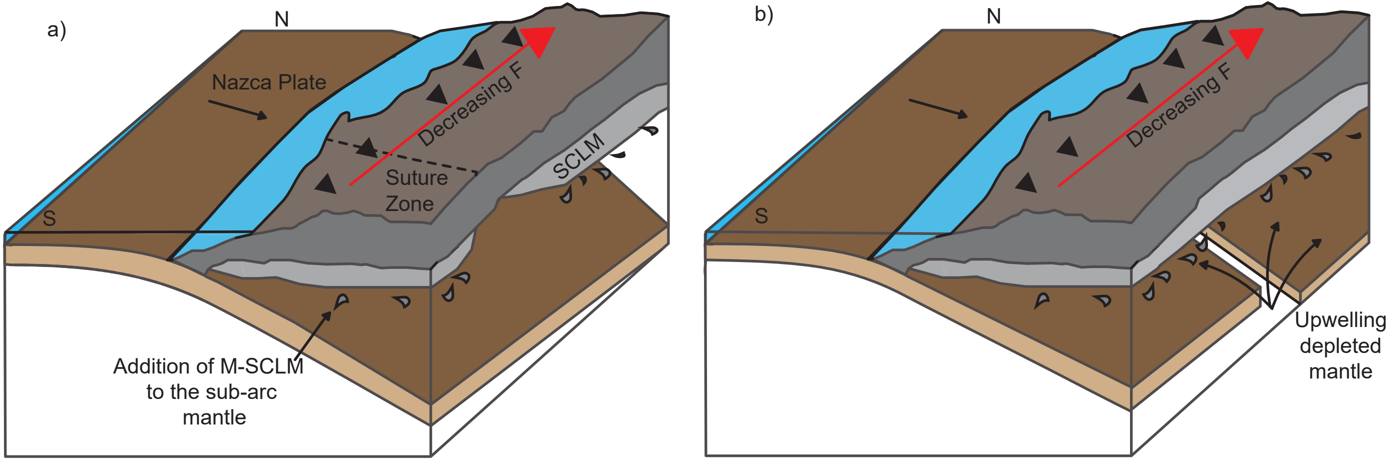
a)
N
Nazca Plate
S
Decreasing F
Suture Zone
SCLM
Addition of M-SCLM to the sub-arc mantle
b)
N
S
Decreasing F
Upwelling depleted mantle

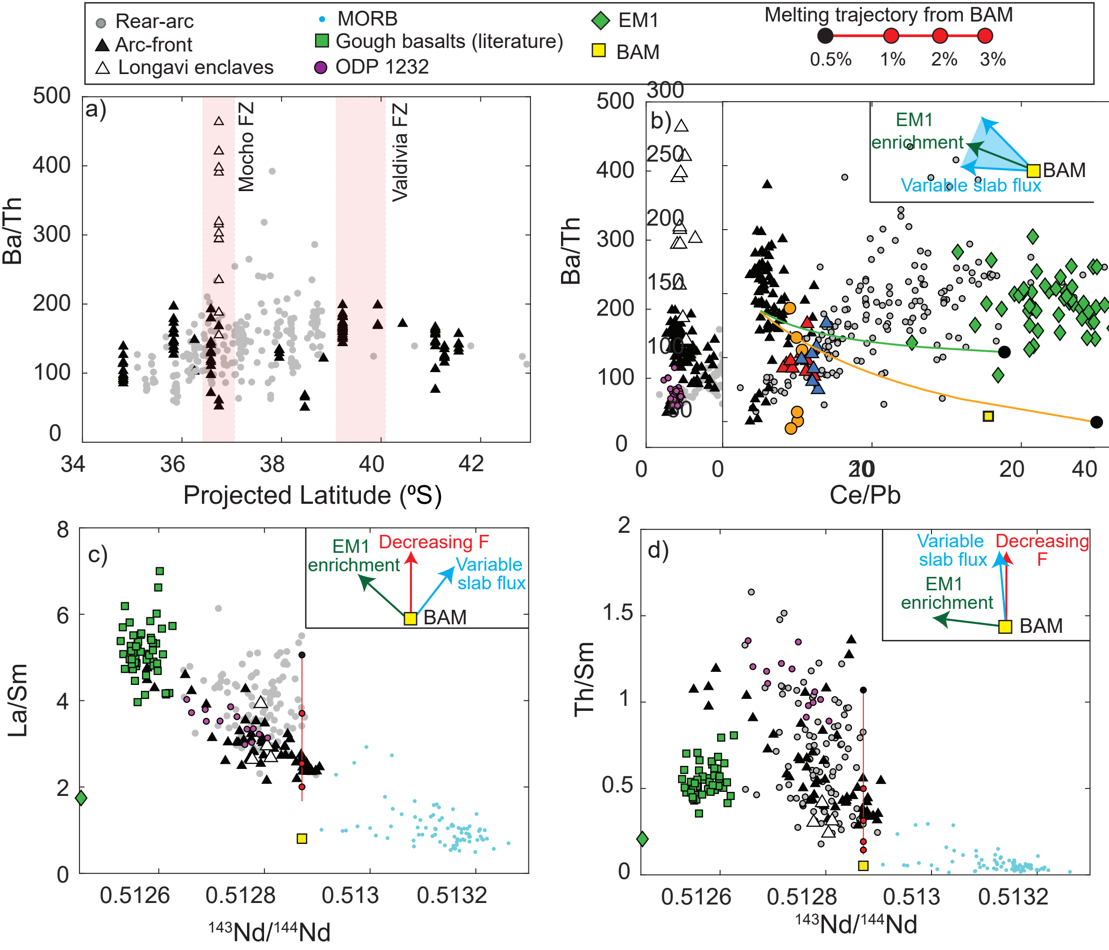

Rear-arc
Arc-front
Longavi enclaves
MORB
Gough basalts (literature)
ODP 1232
EM1
BAM
Melting trajectory from BAM
0.5%
1%
2%
3%
a)
Mocho FZ
Valdivia FZ
Ba/Th
500
400
300
200
100
0
34
36
38
40
42
Projected Latitude (ºS)
b)
300
250
200
150
100
50
0
EM1
enrichment
Variable slab flux
BAM
Ba/Th
500
400
300
200
100
0
10
20
40
Ce/Pb
c)
EM1
enrichment
Decreasing F
Variable
slab flux
BAM
La/Sm
8
6
4
2
0
0.5126
0.5128
0.513
0.5132
$^{143}Nd/^{144}Nd$
d)
Variable
slab flux
Decreasing
F
EM1
enrichment
BAM
Th/Sm
2
1.5
1
0.5
0
0.5126
0.5128
0.513
0.5132
$^{143}Nd/^{144}Nd$

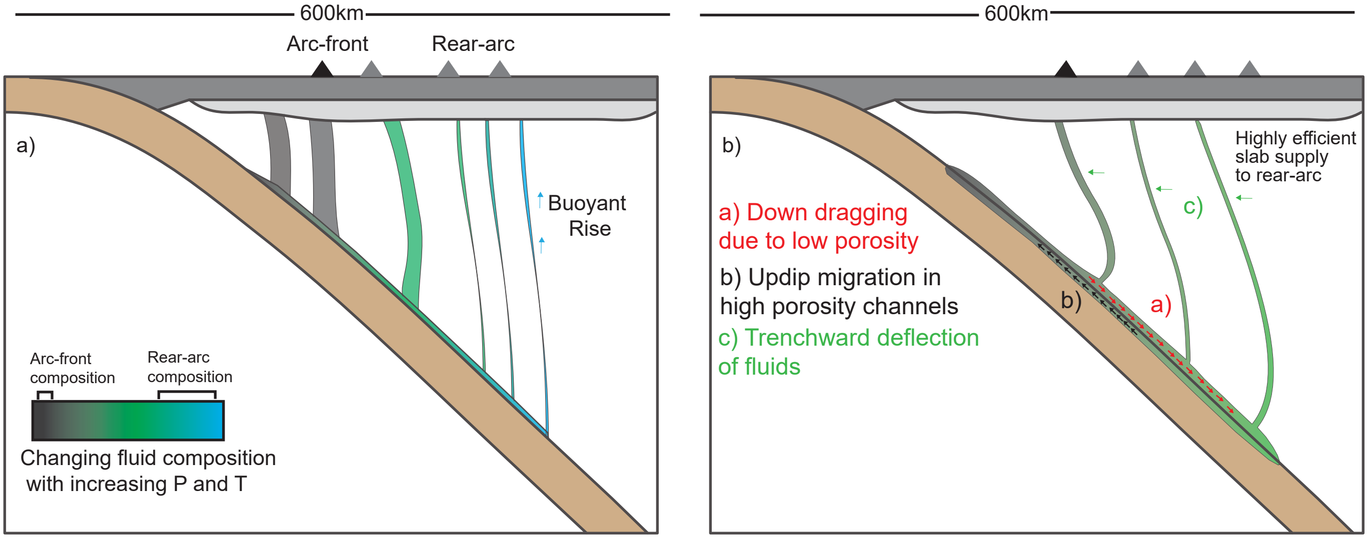
600km
Arc-front
Rear-arc
a)
Buoyant Rise
Arc-front composition
Rear-arc composition
Changing fluid composition with increasing P and T
600km
b)
Highly efficient slab supply to rear-arc
a) Down dragging due to low porosity
b) Updip migration in high porosity channels
c) Trenchward deflection of fluids
c)
b)
a)

Appendix 1: Methods and Sample Details

SIA1 Data and Databases

Whole-rock and olivine analysis from this study is shown in Appendix 3. Compiled rear-arc and Diamante-Maipo literature data used in this study is in Appendix 4. The compilation of SVZ basement compositions is in Appendix 5.

SIA2 Sample Characteristics

Six 100μm sections were made for Don Casimiro-Maipo samples spanning a range of MgO contents. These were scanned using a 5MP slide scanner. Point counting was conducted in JMicroVision by overlaying a 1000 point grid on these scans. Microscope observations were made on any crystals that couldn't be identified with certainty in scans. Crystals smaller than ~0.05mm were classified as matrix. Amorphous or crystalline material sufficiently distinct from the surrounding matrix that could not be identified as a mineral phase was classified as alteration.

Table SA1: Point counting results for Don Casimiro-Maipo samples (ordered by decreasing wt% MgO).

Sample	MgO (wt%)	Crystals (%)	Matrix (%)	Vesicles (%)	Alteration (%)
G0020315-1	6.82	11	89	0	0.1
G0020315-2	6.73	10	90	0	0.3
G0270215-1D	5.63	17	81	0	0.3
G0270215-1C	4.85	14	85	0	0.2
G0030315-4	3.87	11	72	16	0.0
G0030315-1	2.99	42	48	0	10

Table SA2: Percentage of each phenocryst phase in the crystal fraction. *The fine grained nature of these samples meant that phenocryst phases were harder to identify, so proportions are not as reliable as for other samples.

Sample	Olivine (%)	Clinopyroxene (%)	Plagioclase (%)	Oxide (%)	Orthopyroxene (%)
G0020315-1	66	34	0	0	0
G0020315-2	66	34	0	0	0
G0270215-1D*	6	15	46	33	0
G0270215-1C*	8	20	32	41	0
G0030315-4	7	5	89	0	0
G0030315-1	3	13	82	0	3

Table SA3: Description of Don Casimiro-Maipo samples in thin section.

Sample	Olivine	Plagioclase	Clinopyroxene	Matrix Textures
G0020315-1	Predominantly subhedral-anhedral 2-0.5mm grains, and smaller, <0.5mm anhedral grains. Both types form clots, and show association with clinopyroxene. Most olivines contain oxide inclusions.	No phenocrysts.	Subhedral-anhedral 2-0.5mm grains, often forming clots. Smaller, <0.5mm anhedral grains within the matrix. Some show breakdown in their cores.	Dark, fine grained matrix with white streaks of amorphous material. Needle-shaped matrix plagioclase aligns with these streaks. A few 1-2mm patches of alteration are associated with reacted olivine cores.
G0020315-2	Euhedral 1-3mm grains, subhedral 0.5-2mm clots associated with clinopyroxene, and smaller isolated <1mm anhedral grains.	No phenocrysts.	Subhedral 1-2mm grains, often associated with olivine clots. As above, some show broken down cores.	Dark, fine grained matrix, with white amorphous material in streaks. Small needle-shaped plagioclase shows alignment around large crystals. Abundant anhedral oxide grains.
G0270215-1D	Anhedral <0.2mm grains with abraded edges. These are associated with patches of small red amorphous material.	Blocky to needle-shaped plagioclase. No alignment.	Sub-anhedral, 0.3-1mm grains. These are more commonly associated with the red material than olivines.	Dark, fine grained matrix, with poorly aligned, needle-shaped plagioclase, and dispersed anhedral oxides. Patches of white, amorphous material.
G0270215-1C	Anhedral, <0.1mm grains.	Elongated needles, 20:1 aspect ratio. Aligned in matrix.	Sub-anhedral 0.3-1mm grains, associated with red amorphous material and oxide growth.	Dominated by small, aligned, needle-shaped plagioclase, with euhedral-anhedral opaque oxides.
G0030315-4	Anhedral, <1mm grains, with highly abraded edges, likely these were originally clots.	Large, 2mm+, blocky plagioclase, showing sieve textured cores (indicating rapid growth/cooling/heating).	Euhedral, 2-4mm grains, and smaller, <1mm highly abraded anhedral grains.	Highly vesicular texture. Matrix dominated by glass.
G0030315-1	A few subhedral, 1-2mm olivines. Some associated with large, 1-2mm cubic oxide phases.	Several populations of plagioclase. 1) blocky 2-4mm rectangular macrocrysts, with large fluid inclusions. 2) lath shaped 1-3mm grains, with inclusion-free cores. 3) needle shaped (<1mm) grains, with sieve textured cores.	Euhedral-subhedral, 1-2mm grains with oxide inclusions. Some are also associated with very large, 1-3mm oxide grains. Additionally, one 4mm clot of several grains and oxides is observed. In some places, clinopyroxene forms anhedral intergrowths with plagioclase, and orthopyroxene.	Extremely crystal-rich. Large areas of amorphous material within the slide are associated with large blocky plagioclase macrocrysts. Between phenocrysts, the matrix is dark and amorphous.

SIA3 Methodologies

SIA3.1 Whole Rock Chemistry

Sixteen samples from Don Casimiro-Maipo and seven rear-arc samples were prepared for whole-rock analysis at the University of Oxford. Arc-front lava samples were cleaned in an ultrasonic bath until the water ran clear. These were then split into 2-3cm chunks using a pneumatic rock splitter. Rear-arc samples were wet sieved, and unaltered clasts from the coarsest fraction (>2mm) were hand picked for whole rock analysis. Both sample types were crushed in a steel jaw crusher, and then powdered in an agate ball mill.

Major Element Analysis: Major element analyses was conducted by using a PANalytical Axios Advanced X-ray fluorescence spectrometer at the University of Leicester, UK, following the methods of Knott et al. (2016).

Trace Element Analysis: ∼ 100 mg of each powder as well as reference materials BCR-2a, BHVO-2, W-2a and AGV-2, were digested in ∼4ml of 7.5M HNO_3 and ∼1ml of 24M HF. The samples where then evaporated and redissolved twice in ∼4ml 7.5M HNO_3 to eradicate fluoride precipitates. At this stage, a sample split was made for isotopic analysis. Trace element analyses were conducted using a Perkin Elmer NexION 350D quadrupole ICP-MS for the majority of elements. An additional 1200x dilution and addition of an internal standard containing Rh, Re, and In was achieved using the ESI prepFAST system producing a 6000x solution in which to measure lower concentration elements. All prior dilutions were performed gravimetrically. Sample G0030315-4 was run every four samples, and the entire run was duplicated in reverse order to monitor drift. Drift correction and data reduction were carried out following Turner et al. (2013). Due to malfunctioning of the Prepfast system, a planned run at 60,000x dilution for higher concentration elements using the same method failed. Thus, Sr and Ba concentrations were measured using a Thermo Element 2 ICP-MS (also at the University of Oxford) at a 1,200,000x dilution (performed gravimetrically).

The digestion procedure, and sample homogeneity can be assessed by calculating the % difference between the measured element concentrations of two duplicates produced from the powders of this study, and two from an additional set of samples digested alongside these. Most measurements lie within 5%, suggesting that the digestion process, and samples, were reasonably homogeneous (table SA4).

Isotopic Analysis

Strontium (Sr) and neodymium (Nd) isotope analyses were performed on a Thermo Scientific Triton-series multicollector mass spectrometer at the School of Earth and Environment, University of Leeds. Eleven whole-rock powders were digested alongside those for trace element analysis, followed by subsequent drying and pick up in concentrated ultrapure HNO_3 and HCl acids. The final dried samples were diluted and centrifuged for 15 minutes at 2000 rpm. Sr and Nd were extracted by using Sr-Spec and TRU-spec resins and conventional ion-exchange chromatographic techniques. $^{87}Sr/^{86}Sr$ and $^{143}Nd/^{144}Nd$ ratios were normalized for mass fractionation to $^{86}Sr/^{88}Sr=0.1194$ and $^{146}Nd/^{144}Nd=0.7219$. Samples for Sr were loaded onto previously outgassed W filaments and samples for Nd were loaded onto previously outgassed Re filaments. Sr and Nd were analysed while the current was maintained between 3-5 V (for ^{88}Sr) and 0.4-0.8 V (for ^{144}Nd).

The average $^{87}Sr/^{86}Sr$ obtained from repeated measurements of NIST SRM-987 during the course of this study was 0.710271. Similarly, we measured $^{143}Nd/^{144}Nd=0.511837$ for the LaJolla standard. Two samples (G0020315-2 and G0270215-1C) were analyzed for $^{143}Nd/^{144}Nd$ in a separate run, in which we measured $^{143}Nd/^{144}Nd=0.511850$ for the LaJolla standard. We also successfully reproduced the published USGS standard BHVO-2 values for $^{87}Sr/^{86}Sr=0.703468$ and $^{143}Nd/^{144}Nd=0.512995$ (Weis et al., 2005). Details on the sample preparation and analytical protocols are described in Crummy et al. (2014).

SIA3.2 Correction of Isotopic data of this study and Literature Data

Sr and Nd isotopes from the literature and this study were corrected to be in line with the analytical procedure used for SVZ data presented in Turner et al. (2016). Various standards were corrected to be equivalent to La Jolla=0.511858, NBS 987=0.710235 based on session averages.

Table SA4: % deviation of four duplicates ran during analysis on the "quad" (except starred elements, where % deviation is reported from the "element"). (4) represents a duplicate of G0030315-4, (1) represents a duplicate of MDZ1, 079a and B1 are samples measured in the same run, but for use in a study on the Main Ethiopian Rift. % deviation is defined as (Measurement 1-Measurement 2)/(Average of measurement 1 and 2) x 100.

	% difference (4)	% difference (1)	% difference (079)	% difference (B1)
Li	4.13	1.74	-0.97	0.35
Be	-4.52	60.2	-12.4	1.29
Sc	5.89	-27.0	-20.5	-0.72
V	2.02	-1.95	-0.65	0.15
Cr	3.02	0.41	1.14	-0.99
Ni	3.53	0.74	0.86	1.47
Cu	4.71	-3.94	-0.26	1.76
Rb	3.64	0.28	-9.66	0.30
Sr*	5.54	1.74	0.35	-5.67
Y	2.99	-3.08	-6.18	-0.94
Zr	2.12	-0.29	-0.42	0.32
Nb	3.09	0.21	-0.30	1.16
Cs	8.90	-5.49	-4.43	9.11
Ba*	6.08	3.17	3.65	-2.89
La	3.52	0.58	1.10	0.82
Ce	3.31	-1.09	0.94	0.70
Pr	4.57	0.71	2.05	0.80
Nd	3.29	3.63	-0.88	-0.53
Sm	0.00	2.17	1.35	2.23
Eu	2.21	2.20	1.55	-1.12
Gd	3.09	-2.92	-2.87	1.04
Tb	3.26	-2.17	2.29	0.91
Dy	3.83	-0.60	2.67	0.78
Ho	4.64	-2.73	-0.32	3.88
Er	2.99	4.01	-2.53	3.70
Tm	2.81	-5.67	-3.75	0.51
Yb	2.67	1.49	-0.23	1.69
Lu	1.28	1.41	-3.58	1.15
Hf	3.34	0.93	-0.87	1.40
Ta	-2.98	-0.57	1.60	-0.94
Pb	3.55	-2.14	-9.60	1.72
Th	3.48	-2.05	-17.6	-1.10
U	3.33	-0.09	0.56	-0.11

SIA3.3 Olivine Chemistry

Olivines were picked from the 1000-250μm grain fractions, and mounted in epoxy rings. These mounts were polished and carbon coated for EMPA analysis. Analysis was conducted with an accelerating voltage of 15KeV, a current of 100nA and a 10μm spot size. St John's Island and Fayalite were run as secondary standards, with % recoveries reported in table SA5.

LA-ICP-MS analysis was conducted at the University of Cambridge. Three instrument runs were performed over two days. The run conditions were 20Hz, 80µm, 9.5J/cm^2, 0.8L/min of gas flow for He and Ar. Where possible, three spots were placed in the centre of the olivine, with no overlap. For very small grains, only 2 spots were placed, as it is preferable to have fewer spots nearer the centre than more spots towards the grain edges, due to the reasonably high diffusivity of elements of interest to this study. To allow drift correction, 3 spots on each of

NISTSRM612, NISTSRM610, 06SGOL03 (inhouse olivine standard) and BD4074OL-7 (a San Carlos olivine) were run every 30 analyses. ^{29}Si was used as an internal standard, with values obtained from EMPA grain averages. Signals were selected using Glitter Processing software, with normalization to NISTSRM612 via a quadratic drift correction. This was effective at removing drift, as determined by observing the stability of NISTSRM610, 06SGOL03 and BD4074OL-7 following this correction. Multiple secondary standards were run to assess the accuracy of the measurement for elements of interest (NISTSRM610, NISTSRM614, BCR-2G). Measurement of inhouse olivines O6SGOl03 and BD407OL-7 provided an excellent assessment of the success of the drift correction performed on glass standards. Elements of interest in this study drifted by less than 7%. Although Mn and Ni recovery on glass standards were good, these elements were recovered more poorly on BCR-2G. This, and the fact that previous studies in this area have used EMPA Ni and Mn data, resulted in us choosing to use EMPA data for consistency, as most of the peridotite-pyroxenite ratios involve normalization to Fe (which is reported from EMPA). Detection limits, and 1 sigma uncertainties calculated from Glitter for a representative sample (MDZ2) are shown in table SA6.

Table SA5: Peak count times, and calibration materials used. % recovery calculated below is defined as Measured Average/Published Average x 100. Where no published value exists for a standard, - is shown. Detection limits are reported from 9 spots on MDZ8. These are assumed to be representative of the analysis as a whole.

	Mn	Fe	Mg	Si	Ca	Ni
Peak count times (s)	20	30	20	20	70	70
Calibration material	Mn metal	Andradite	MgO	Albite	Wollastonite	Ni metal
% Rec Fayalite	97.7	94.2	-	99.6	97.0	-
% Rec St Johns Island Olivine	106.1	96.1	99.6	99.2	-	90.1
Detection limit (ppm)	173	197	173	98	74	137

Table SA6: Minimum (99% Confidence) detection limits (ppm), and 1 sigma uncertainties (ppm) for all spots on MDZ2, taken as representative for the analysis as a whole. The mass in brackets represents the isotope measured on the ICP-MS.

Element	MDL	1 σ uncertainty
Li(7)	0.115	0.151
Na(23)	1.121	6.92
Al(27)	0.318	39.3
P(31)	13.76	47.3
Ca(43)	133	192
Sc(45)	0.062	0.412
Ti(47)	0.551	18.4
V(51)	0.043	0.504
Cr(53)	0.578	56.0
Mn(55)	0.136	88.4
Co(59)	0.049	7.91
Ni(60)	0.171	191
Cu(65)	0.351	0.416
Zn(66)	0.373	10.1
Ga(69)	0.042	0.049
Ge(72)	0.370	0.208
Y(89)	0.037	0.025
Zr(90)	0.033	0.052
Nb(93)	0.035	0.021

Table SA7: % recovery of NISTSRM610 (average of 3 spots). (x,y) refers to when this secondary standard was run, x referring to the instrument run (1-3), and y to the order of measurement within a given run. These values were used to check the success of the quadratic drift correction. Across the three instrument runs, most elements drift by less than 10%.

Element	(1,1)	(1,2)	(1,3)	(1,4)	(1,5)	(2,1)	(2,2)	(2,3)	(2,4)	(3,1)	(3,2)	(3,3)	(3,4)	AVERAGE
Li(7)	98.0	105.5	103.7	106.7	105.9	107.3	104.3	101.1	103.6	108.0	99.6	96.8	98.2	103.0
Na(23)	98.2	105.7	107.0	106.1	105.9	105.9	104.9	101.4	103.9	105.0	103.0	101.1	102.1	103.9
Al(27)	102.3	105.5	105.9	106.2	107.8	108.3	104.2	104.9	107.3	105.6	107.2	103.5	104.9	105.7
P(31)	107.8	105.2	99.7	130.9	194.5	100.5	103.9	101.0	100.5	125.0	113.1	117.6	133.9	118.0
Ca(43)	95.9	103.7	100.6	106.7	107.3	105.2	102.5	99.2	102.2	105.2	100.1	99.5	104.5	102.5
Sc(45)	98.7	109.1	108.0	109.8	108.8	110.2	110.9	105.6	108.9	108.5	106.7	108.0	109.6	107.9
Ti(47)	115.2	120.8	116.9	120.0	119.0	125.1	128.7	124.5	125.5	125.3	125.9	122.8	125.4	122.7
V(51)	95.7	101.9	100.1	105.2	105.8	104.8	102.6	100.1	105.1	105.9	101.7	99.9	103.7	102.5
Cr(53)	103.4	107.7	109.4	113.6	119.5	120.7	115.9	112.1	115.1	114.1	111.4	112.7	116.7	113.2
Mn(55)	94.6	100.0	100.0	103.7	102.4	105.1	100.2	99.0	103.5	104.9	97.1	96.1	97.7	100.3
Co(59)	95.5	103.0	101.7	103.7	100.8	104.2	102.0	98.9	104.3	103.6	101.0	100.3	103.4	101.7
Ni(60)	92.1	100.9	99.8	103.7	99.9	105.6	100.1	98.2	100.0	104.3	101.8	100.5	102.2	100.7
Cu(65)	89.9	98.8	97.3	100.1	97.5	100.5	98.4	94.9	99.0	100.1	96.0	95.9	97.6	97.4
Zn(66)	98.5	104.1	102.3	108.8	110.2	111.1	104.4	100.1	106.6	109.9	106.4	104.1	102.9	105.3
Ga(69)	92.2	97.7	96.5	101.1	101.5	101.7	99.0	97.2	99.4	101.4	98.9	98.3	100.8	98.9
Ge(72)	81.5	86.7	85.7	89.1	88.8	92.4	89.0	85.6	86.6	92.0	87.5	87.8	89.8	87.9
Y(89)	93.1	102.1	99.8	102.8	102.1	104.0	102.9	100.5	100.3	102.5	101.4	101.8	103.8	101.3
Zr(90)	89.8	95.9	94.6	97.9	98.1	98.6	98.5	94.6	95.4	97.5	96.8	96.0	98.7	96.3
Nb(93)	92.8	99.9	98.9	102.4	101.7	102.2	102.2	98.1	100.2	102.9	99.9	99.2	101.1	100.1

Table SA8: % recovery of BCR-2G, using averages from 3 spots, and % recovery of NISTSRM614. The % recovery for NISTSRM614 is not shown for the first run. These were the first spots ran by the laser, and it has been shown that the system takes a few spots to warm up and settle after switching from solution mode to laser mode.

Element	(1,1)	(2,1)	(2,2)	(3,1)	(3,2)	BCR-2G Average	(2,1)	(3,1)	NISTSRM614 Average
Li(7)	100.2	104.5	101.7	105.8	94.6	101.4	84.4	103.7	94.1
Na(23)	96.2	99.1	97.0	101.4	96.9	98.1	105.5	103.1	104.3
Al(27)	103.8	103.4	99.9	104.6	103.3	103.0	106.6	106.3	106.4
P(31)	101.3	84.9	86.8	108.4	120.1	100.3	268.2	260.0	264.1
Ca(43)	99.0	97.9	98.9	101.1	99.1	99.2	106.2	103.7	105.0
Sc(45)	97.5	102.1	96.4	100.8	99.9	99.3	217.1	185.9	201.5
Ti(47)	107.3	108.4	105.2	110.9	106.3	107.6	122.1	101.3	111.7
V(51)	97.6	100.1	101.1	102.8	99.6	100.2	109.7	99.9	104.8
Cr(53)	93.2	104.4	92.9	97.1	101.1	97.7	94.8	113.0	103.9
Mn(55)	92.4	96.6	94.9	98.5	90.0	94.5	105.6	89.7	97.7
Co(59)	99.0	97.8	97.0	97.9	96.2	97.6	92.6	95.0	93.8
Ni(60)	89.4	86.9	83.8	90.2	86.5	87.4	107.9	71.8	89.8
Cu(65)	71.0	72.5	67.5	71.1	69.6	70.3	88.8	109.0	98.9
Zn(66)	121.5	134.0	127.4	134.9	120.7	127.7	91.4	89.2	90.3
Ga(69)	111.6	117.1	109.2	118.4	114.5	114.2	96.9	93.9	95.4
Ge(72)	99.6	112.9	95.6	101.1	102.4	102.3	86.3	110.8	98.5
Y(89)	87.3	90.0	81.9	90.6	89.1	87.8	102.0	99.4	100.7
Zr(90)	84.5	87.0	78.3	87.7	86.3	84.7	90.3	91.6	90.9
Nb(93)	88.6	91.6	86.6	91.0	90.2	89.6	93.7	99.3	96.5

SIA4 Mantle Melting Model Details

As discussed in the text, this study uses an updated version of the model of Turner and Langmuir (2015b). Below, the justification of various inputs to the model are discussed. The updated Matlab scripts ADD_SLAB.m, ADD_SLAB_HOTP.m and ModeMelt_Hydrous.m have been uploaded into the supplementary information.

SIA4.1 Model Partition Coefficients

Hydrous Partition Coefficients for Mantle Melting: This study utilizes hydrous partition coefficients and mantle modes from Turner and Langmuir (2015b; detail in their supplement). However, we slightly updated the partitioning behaviour of several elements:

1) The bulk partition coefficient of Eu is obtained by a log extrapolation from those of Sm and Gd:

$$\mathrm{Kd}_{Eu} = (\mathrm{Kd}_{Sm}{*}\mathrm{Kd}_{Gd})^{0.5}$$

correcting an error in Turner and Langmuir (2015b).
2) The partition coefficient of Hf is assumed to be equal to that of Sm.
3) The partition coefficient of Zr is approximated as:

$$\mathrm{Kd}_{Zr} = (\mathrm{Kd}_{Nd}{*}\mathrm{Kd}_{Sm})^{0.5}$$

Hydrous Partition Coefficients for slab melting: As above, this study uses slightly adapted partition coefficients for slab melting to those in Turner and Langmuir (2015b). These lie within the limits of experimental values (figure SA1). The partition coefficients for the LREE (La, Ce, Nd, and Sm) were reduced by 40% to reflect the hotter slab underneath Don Casimiro-Maipo (inline with experimental high temperature partitioning results; figure SA1). Additionally, the partition coefficients of Zr and Hf were reduced, and 70% of Cs was assumed to be lost to the forearc.

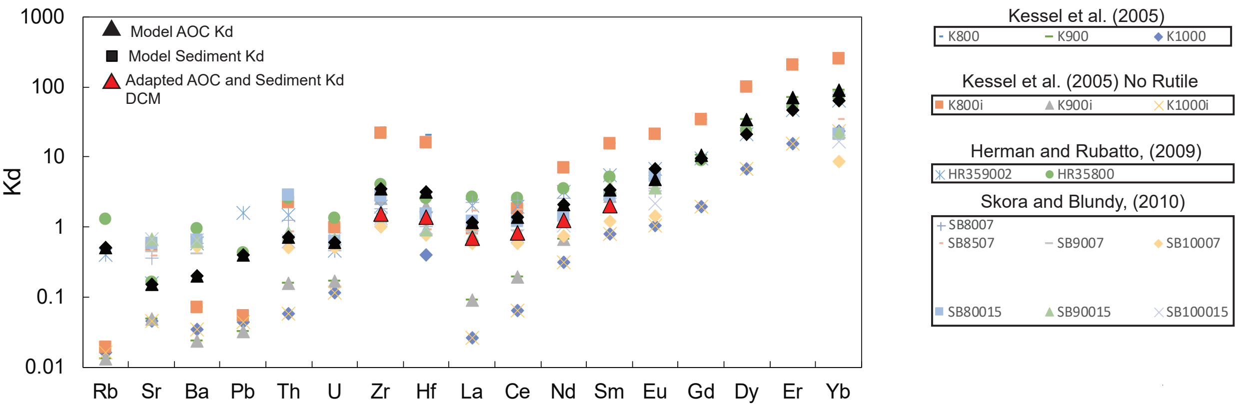

Figure SA1: Slab melting partition coefficients lie within experimental values for 800-1000°C.

SIA4.2 Model End-Members

"Ambient Andean Mantle" (Depleted Mantle End-Member): The isotopic composition of the depleted mantle end member was set to ^{87}Sr/^{86}Sr=0.70355 and ^{143}Nd/^{144}Nd=0.512871, the isotopic composition of sample 126171 of Soager et al. (2013) following the isotopic correction discussed above. This sample lies at the depleted end of the rear-arc array, and thus reflects the composition of the Andean mantle prior to the addition of EM1 enrichment. For trace element modelling, the depleted mantle end-member is DMM of Workman and Hart (2005).

AOC: The subducting Nazca plate has Pacific affinities. Trace element concentrations were obtained from melting of N-MORB (Gale et al., 2013) at 876°C, F=0.3. The isotopic composition of AOC was set to ^{87}Sr/^{86}Sr = 0.7035, ^{143}Nd/^{144}Nd = 0.5130.

Sediment: The trace element composition of the sediment end-member was obtained from 33 samples of ODP1232 (c.f. Turner et al., 2017). To produce an envelope of model results for trace elements and isotopes, one standard deviation of measured samples were added and subtracted to the mean. Three outliers were discarded based on their anomalously high Sr isotope ratios.

Enriched EM1 end-member: Enrichment at Gough represents a mix of M-SCLM, and ambient mantle. The isotopic signature of recycled M-SCLM depends on the storage time (Turner et al., 2017). As several samples within this study have signatures more enriched than Gough, we use the isotopic composition of a sample from Pitcairn (57DS9; Stracke et al., 2003) as the EM1-like isotopic end member. This lies at the enriched end of the field enclosing EM1-type ocean island basalts. The trace element concentration was obtained from the inversion of Turner et al. (2017), with a few changes:

1) the bulk Eu partition coefficient was set at:

$$\mathrm{Kd}_{Eu} = (\mathrm{Kd}_{Sm}{*}\mathrm{Kd}_{Gd})^{0.5}$$

correcting an error in Turner et al. (2017) where it was set at 0.

2) The Zr concentration in Gough primary melts was adjusted to the standard EM1 value Zr/Hf = 45.

3) Zr partition coefficients were extrapolated from Salters and Longhi (1999).

4) Nb and Ta partition coefficients were taken as $\mathrm{Kd}_{La}/3$, based on ratios from Workman and Hart (2005).

Table SA9: Gough mantle source composition used in this study compared to that of Turner et al. (2017; T2017).

	Eu	Zr	Nb	Ta
This study	0.130	6.70	0.403	0.024
T2017	0.0234	11.47	0.472	0.028

SIA5 References

Crummy, J., Savov, I.P, Navarro-Ochoa, C., Morgan, D., Wilson, M., 2014. High-K mafic Plinian eruptions of Volcán de Colima, México, Journal of Petrology, 55 (10). pp.1-18.

Kessel, R., Schmidt, M.W., Ulmer, P. and Pettke, T., 2005. Trace element signature of subduction-zone fluids, melts and supercritical liquids at 120–180 km depth. Nature, 437(7059), pp.724-727.

Knott, T.R., Branney, M.J., Reichow, M.K., Finn, D.R., Coe, R.S., Storey, M., Barfod, D. and McCurry, M., 2016. Mid-Miocene record of large-scale Snake River–type explosive volcanism and associated subsidence on the Yellowstone hotspot track: The Cassia Formation of Idaho, USA. Bulletin, 128(7-8), pp.1121-1146.

Roduit, N. JMicroVision: Image analysis toolbox for measuring and quantifying components of high-definition images. http://www.jmicrovision.com (accessed 4th January 2017).

Salters, V. and Longhi, J. (1999). Trace element partitioning during the initial stages of melting beneath mid-ocean ridges. Earth and Planetary Science Letters 166: 15-30. doi: 10.1016/S0012-821X(98)00271-4.

Turner, S.J., Izbekov, P. and Langmuir, C., 2013. The magma plumbing system of Bezymianny Volcano: Insights from a 54 year time series of trace element whole-rock geochemistry and amphibole compositions. Journal of Volcanology and Geothermal Research, 263, pp.108-121.

Weis, D., Kieffer, B., Maerschalk, C., Pretorius, W., Barling, J. 2005. High-precision Pb-Sr-Nd-Hf isotopic characterization of USGS BHVO-1 and BHVO-2 reference materials. Geochemistry Geophysics Geosystems, 6, Q02002.

Appendix 2

SIB1 Evidence for AFC processing

As mentioned briefly in the main text, when samples from the entire Diamante-Maipo caldera complex are considered, the correlations between $^{87}Sr/^{86}Sr$ and $^{143}Nd/^{144}Nd$ and indices for fractionation and assimilation (MgO and Eu/Eu*) provide strong evidence for AFC (figure SB1)

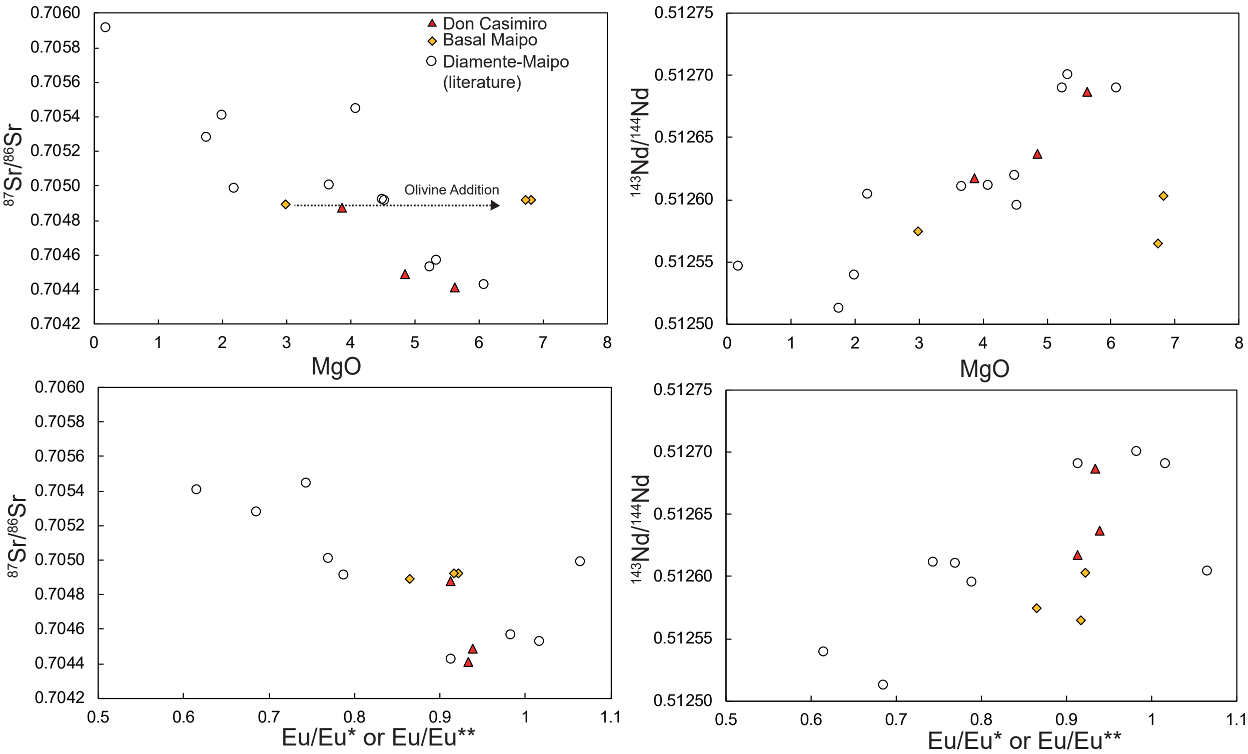

Figure SB1: Within the Diamante-Maipo Caldera, isotopic enrichment increases with assimilation and fractionation. The signal of olivine addition for the two most primitive Maipo samples is also clear.

SIB2 Evidence for Olivine Addition

EMPA analysis indicates that Don Casimiro-Maipo olivines lie significantly below the olivine-whole rock equilibrium line (Figure SB2a), indicating excess olivine accumulation. The two most primitive samples, which are from the basal section of Maipo volcano, can be related to the otherwise coherent liquid line of descent among the Diamante Caldera samples by the addition of 7 wt. % Fo 81 olivine (figure SB2b-d.). All samples have phenocrysts of olivine and clinopyroxene, so this trend is not consistent with fractionation of these two phases together. Olivine may have been accumulated from a mush pile produced by fractionation before clinopyroxene appears on the liquidus. This serves as an excellent example of the importance of utilizing individual mineral analyses in conjunction with whole-rock data when interpreting subtle geochemical variations within individual volcanic groups. While it is tempting to represent the parental composition of a volcanic group using the most olivine-phyric samples (6-7vol% olivine, in this case), such samples can often have more complicated petrogenetic histories.

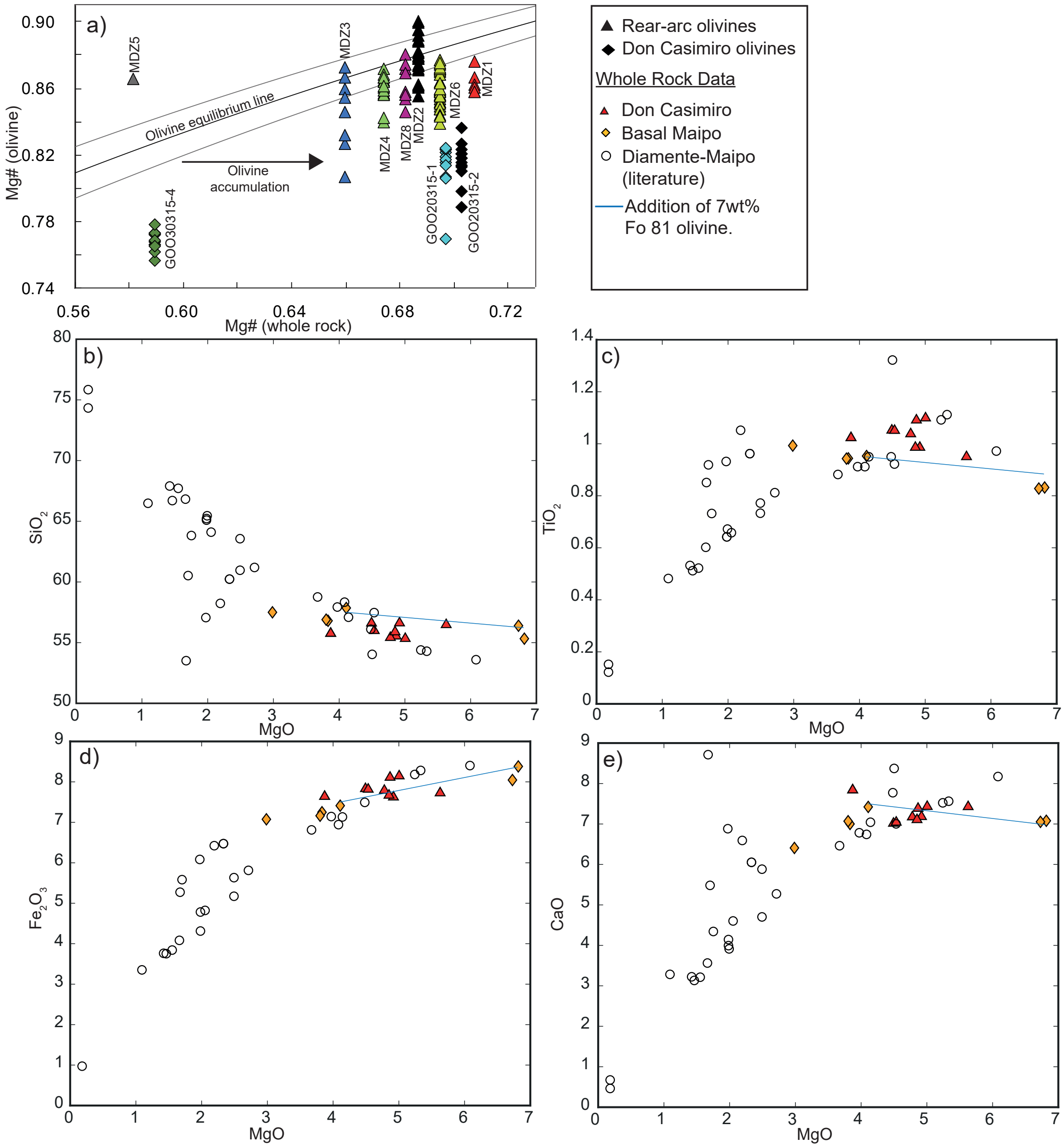

Figure SB2: a) Don Casimiro-Maipo samples show strong evidence for olivine addition, with olivine compositions plotting below an equilibrium line calculated using Roeder and Emslie (1970), Kd=0.3±0.03, assuming whole-rock $Fe^{3+}/Fe_T=0.3$ (Holm et al., 2016). Most rear-arc olivines plot near to or below the equilibrium line, suggesting minor olivine addition (assuming whole-rock $Fe^{3+}/Fe_T=0.15$, Søager et al., 2015b). b-d) Addition of 7 wt% Fo 81 olivine from more evolved Maipo samples produces a good match to the most primitive samples, showing that their high MgO contents are spurious. Diamante-Maipo whole-rock data literature data used in this study is from Hickey et al. (1986), Futa and Stern, (1988), Sruoga et al. (2005), Holm et al. (2014) and Hickey et al. (2016).

SIB3 Changes in Slab Conditions Inferred from Zr-Hf Anomalies

Using Hf/Sm as a proxy, we find that rear-arc and most arc-front volcanics have a similar range of Zr-Hf values, but Don Casimiro-Maipo has a less pronounced Zr-Hf anomaly (figure SB3). The smaller Hf/Sm (and thus Zr-Hf anomaly) at Don Casimiro-Maipo may reflect the fact that the slab is slightly hotter, which causes residual slab zircon to become more soluble in the slab melt (Hirai et al., 2018).

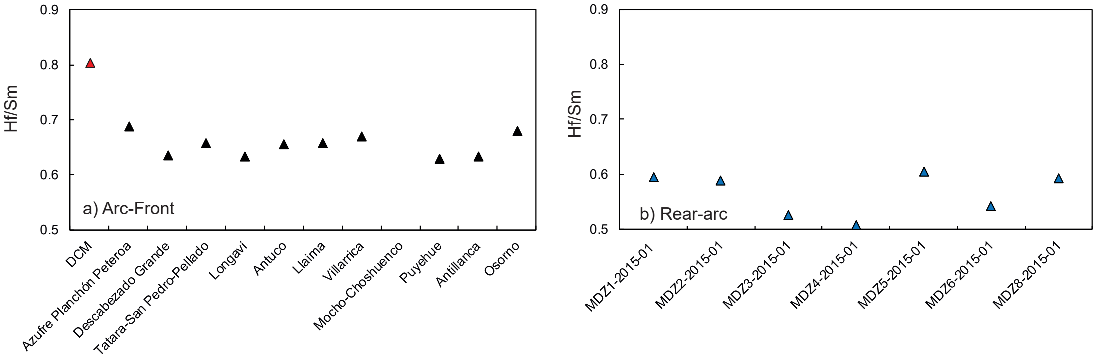

Figure SB3: a) Don Casimiro-Maipo has a significantly different Hf/Sm signature to the rest of the SVZ (data for other centers from Turner et al., 2016). b) Rear-arc centers of this study have similar Hf/Sm ratios to the SVZ arc-front as a whole.

SIB4 Assessing the evidence for LCC assimilation in the SVZ rear-arc

As discussed in section 4.5 of the main text, the offset trajectories of rear-arc and arc-front lavas in trace element and isotope space have been explained by various regional models. We show that these offsets can instead be accounted for a model incorporating variable amounts of EM1 enrichment, combined with variable slab fluxes and melt extents (figure 13 of the main text). This three-parameter model can also account for the offset trajectories in Nd-Hf isotope space (figure SB4). Arc-front and rear-arc lavas both spread along a mixing line between depleted and enriched mantle sources. Arc-front lavas are shifted to the right of the trajectory defined by rear-arc samples due to higher slab fluxes. Additionally, while rear-arc lavas appear to trend towards the composition of LCC xenoliths (Kay et al., 1996) in Ba/Th vs U or Ce/Pb space, calculated mixing lines are hyperbolic, and do not reproduce the trajectory of the rear-arc array (Figure SB5). To accommodate the mis-match between the LCC xenolith mixing model and the rear-arc data, Soager et al. (2013) instead adapt a model LCC composition that has been adjusted for several elements. These adjustments, however, diverge substantially from both global models of the LCC composition as well as the compositional field defined by the larger compilation of Andean basement lithologies (figure SB6).

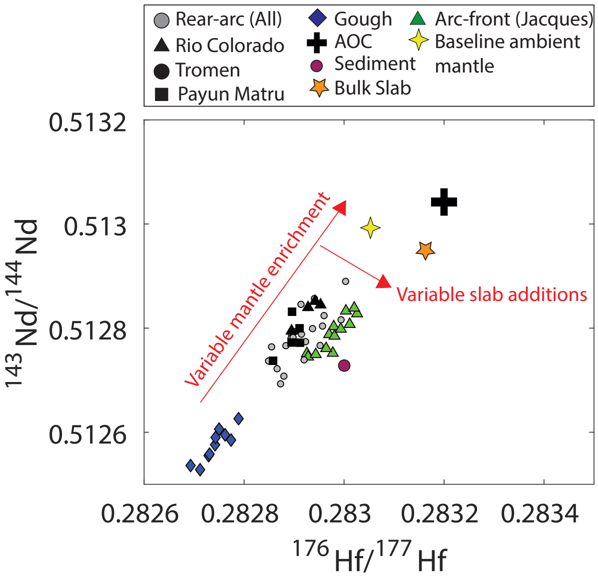

Figure SB4: The offset trends of rear-arc and arc-front lavas in Hf-Nd isotope space can be accounted for a unified model with variable EM1-type enrichment combined with variable slab inputs (see Turner et al., 2017).

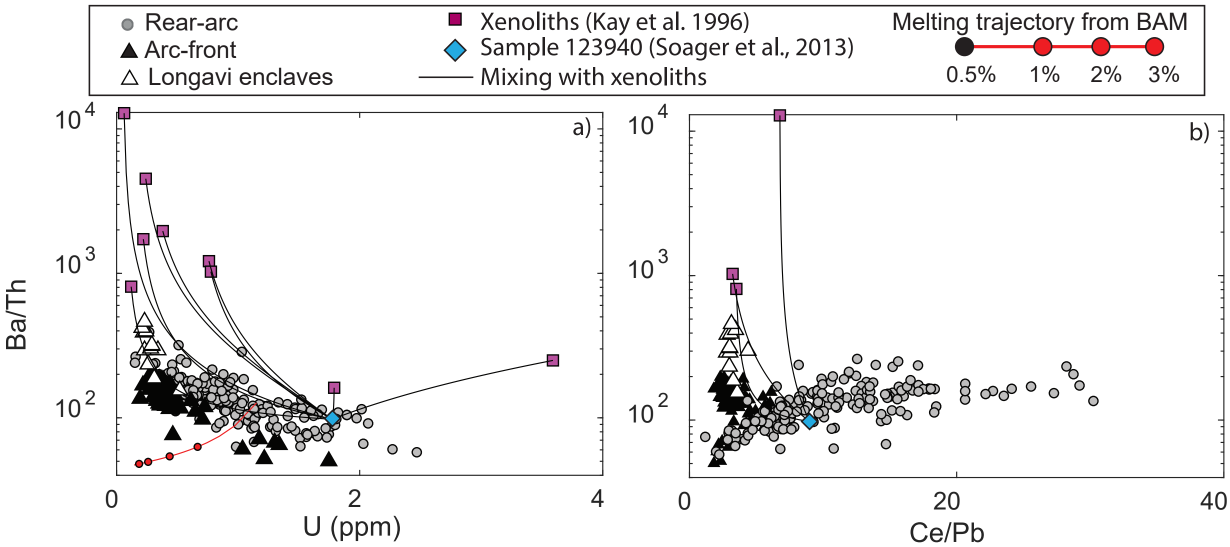

Figure SB5: Soager et al. (2013) suggest that the trajectory of rear-arc lavas trend towards the composition of xenoliths sampled by Kay et al. (1996) in Ba/Th vs. U and Ce/Pb space. However, calculated mixing trajectories between sample 123940 (used in the modelling of Soager et al., 2013) and these xenoliths fail to recreate the rear-arc trends on both plots.

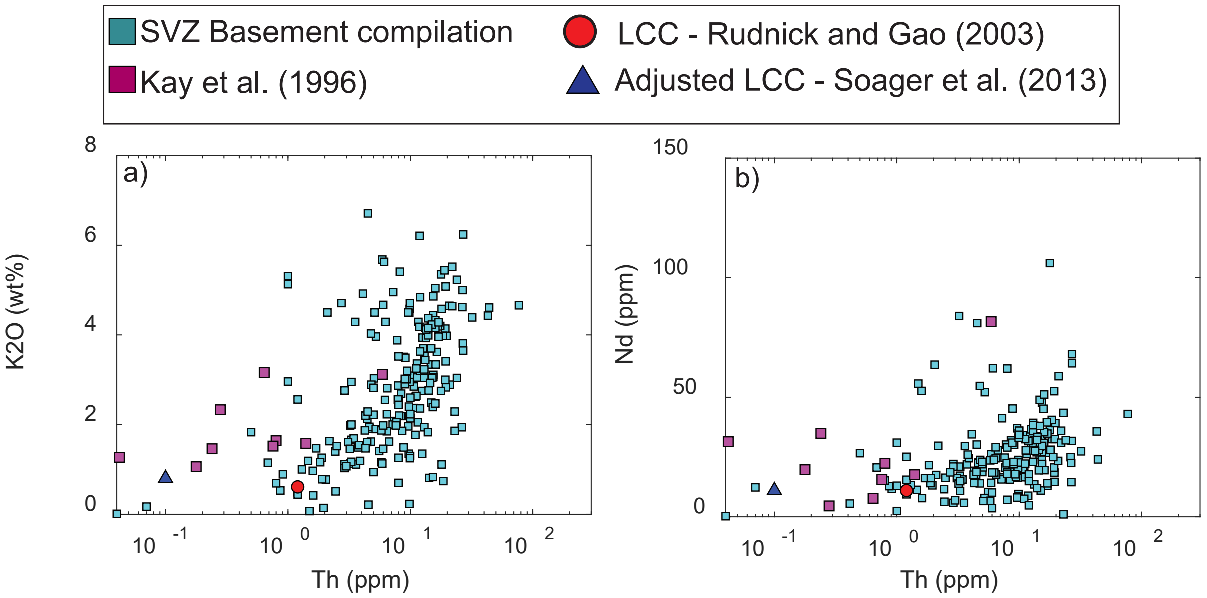

Figure SB6: Comparison of SVZ basement compositions (cyan squares) to the composition of the xenoliths of Kay et al., (1996), the LCC (Rudnick and Gao, 2003), and the basement composition used in the modelling of Soager et al. (2013). It is clear that neither the xenoliths nor the LCC composition of Rudnick and Gao (2003) is particularly representative of the composition of SVZ basement lithologies. Given that the LCC composition of Rudnick and Gao (2003) already deviates substantially from observed SVZ basement lithologies, the adjustments made to the global LCC composition by Soager et al. (2013) are difficult to justify.

References

Roeder, P.L. and Emslie, R., 1970. Olivine-liquid equilibrium. Contributions to mineralogy and petrology, 29(4), pp.275-289.